Hybrid Layered Double Perovskite Halides of Transition Metals

Pratap Vishnoi[a,b], Julia L. Zuo[a], Xiaotong Li[c], Devesh Chandra Binwal[b], Kira E. Wyckoff[a], Ling-ling Mao [a,d], Linus Kautzsch[a], Guang Wu[e], Stephen D. Wilson[a], Mercouri G. Kanatzidis[c], Ram Seshadri[a]*, Anthony K. Cheetham[a,f]*

[a]*Materials Department and Materials Research Laboratory, University of California Santa Barbara, CA 93106, United States of America*

[b]*New Chemistry Unit and International Centre for Materials Science, Jawaharlal Nehru Centre for Advanced Scientific Research (JNCASR), Jakkur P.O., Bangalore 560064, India*

[c]*Department of Chemistry, Northwestern University, Evanston, Illinois 60208, United States of America*

[d]*Department of Chemistry, Southern University of Science and Technology (SUSTech), Shenzhen, 518055 China*

[e]*Department of Chemistry and Biochemistry, University of California, Santa Barbara, CA, 93106 United States of America*

[f]*Department of Materials Science & Engineering, National University of Singapore, 117576 Singapore*

Supporting Information Placeholder

ABSTRACT: Hybrid layered double perovskite (HLDP) halides comprise hexa-coordinated 1+ and 3+ metals in the octahedral sites within a perovskite layer and organic amine cations between the layers. Progress on such materials has hitherto been limited to compounds containing main group 3+ ions isoelectronic with Pb^{II} (such as Sb^{III} and Bi^{III}). Here, we report eight HLDP halides from the $A_2M^IM^{III}X_8$ family, where A = *para*-phenylenediammonium (PPDA), 1,4-butanediammonium (1,4-BDA) or 1,3-propanediammonium (1,3-PDA); M^I = Cu or Ag; M^{III} = Ru or Mo; X = Cl or Br. The optical band gaps, which lie in the range 1.55 eV to 2.05 eV, are tunable according to the layer composition, but are largely independent of the spacer. Magnetic measurements carried out for $(PPDA)_2Ag^IRu^{III}Cl_8$ and $(PPDA)_2Ag^IMo^{III}Cl_8$ show no obvious evidence of a magnetic ordering transition. While the t_{2g}^3 Mo^{III} compound displays Curie-Weiss behavior for a spin-only d^3 ion, the t_{2g}^5 Ru^{III} compound displays marked deviations from the Kotani theory.

Hybrid layered halide perovskites possess useful optoelectronic properties with some appealing characteristics when compared with their 3D analogues. They show greater ambient stability, rich chemical and structural diversity, ease of device fabrication, and exquisite tunability of properties.[1,2] A recent development in the area is the discovery of hybrid layered double perovskite (HLDP) halides, formed by an ordered arrangement of monovalent and trivalent metals in the 2D perovskite layers with large organic amine cations separating and charge-balancing the layers.[3] When diammonium cations separate the layers, Dion-Jacobson (DJ) type structures with eclipsed stacking of the layers are formed in one of the two ways, *i.e.*, [0, 0] or [½, 0] (Figure 1).

Owing to the enormous interest in their optoelectronic properties, 3+ metals that are isoelectronic with Pb^{II}, such as Sb^{III} and Bi^{III}, have been utilized to form a number of HLDP halides. Typical examples include $(1,4\text{-BDA})_2AgBiBr_8$,[4] $(AE_2T)_2AgBiI_8$,[5] $(AMP)_4[AgBiI_8]_2{\cdot}H_2O$,[6] $(CHDA)_2CuBiI_8{\cdot}0.5H_2O$,[7] $(CHDA)_2AgBiI_8.H_2O$,[7] $(MPDA)_2CuBiI_8$,[8] and $(3AMPY)_2AgBiI_8{\cdot}H_2O$ (Table S1).[9–11]

There has separately been considerable progress in the development of layered single perovskite halides of 2+ transition metals (TMs).[12–16] In addition, there is a report of mixed-valence Au^+/Au^{3+} based perovskite iodides containing $[Au^IAu^{III}I_6]^{2-}$ layers of linear $[Au^II_2]^-$ and square planar $[Au^{III}I_4]^-$ ions.[17] However, the family of typical HLDP halides has not yet been extended to heterometallic and magnetic systems with 1+ and 3+ TMs. This could be attributable to synthetic challenges arising from the existence of other oxidation states in addition to the required 1+ and 3+ states. The unfavorable tolerance factors of many of the hypothetical 3D halide perovskites may also impact the ability to synthesize several of the corresponding layered structures.[18]

In terms of magnetic properties, there is great current interest in geometrically frustrated oxides and halides of spin ½ metals. Layered α-$RuCl_3$, with its t_{2g}^5 Ru^{III} configuration and strong spin-orbit coupling (SOC), is an important example of a Kitaev quantum spin liquid.[19] The influence of SOC on the magnetism of Ru^{III} and Ru^{IV} perovskites has also recently been studied.[20,21] These developments have encouraged us to successfully attempt the incorporation of Ru^{III} ($4d^5$) and Mo^{III} ($4d^3$) into eight prototype HLDP halides with the $A_2M^IM^{III}X_8$ composition (Table 1), where A = *para*-phenylenediammonium, 1,4-butanediammonium and 1,3-propanediammonium (hereafter abbreviated as PDA, 1,4-BDA and 1,3-PDA, respectively); M^I = Cu and Ag; M^{III} = Ru and Mo; X = Cl and Br. Their structures, optical properties, and magnetism are discussed below.

The synthesis of the compounds **1** – **8** was accomplished by controlling the oxidation state of the trivalent transition metals by using hypophosphorus acid as a reducing agent.[20] In the absence of H_3PO_2, oxidation of Ru^{III} and Mo^{III} to Ru^{IV} and Mo^{IV} takes place, which prevents the synthesis of the desired products. The compounds are monolayer DJ perovskites comprising fully ordered metal ions and halides in the $[M^IM^{III}X_8]^{4-}$ layers, which are separated by doubly protonated A cations in the stacking direction. The $[M^IX_6]$ polyhedra are distorted with axial compression, while the $[M^{III}X_6]$ polyhedra are nearly regular octahedra. We attribute the smaller distortion around 3+ metal to the stronger M^{III}-X bonds, as well as the large crystal field stabilization energy (CFSE) associated with low-spin M^{III} ions.

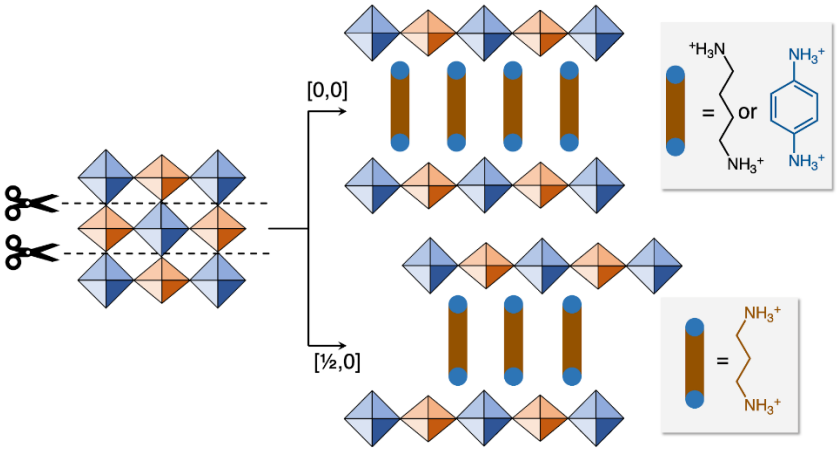

Figure 1. [0, 0] and [½, 0] stacking patterns that can be found in (100) – oriented monolayer DJ HLDP halides. In the former, the successive layers show almost no in-plane displacement, though the layers are eclipsed. They are eclipsed in the latter, too, but consecutive layers show approximately half a unit cell displacement along one of the in-plane axes. The diammonium cations used in this study are also shown.

Table 1. Chemical Composition, Structural Parameters and Optical Bandgaps of the HLDP Halides Described in this Study.

Compound	Stacking pattern	Interlayer spacing (Å)	Symmetry	Glazer tilt system	Bandgap (eV)
$(PPDA)_2AgRuCl_8$ (**1**)	[0, 0]	10.14	Triclinic, $P\bar{1}$	a^-b^-c	1.80
$(PPDA)_2CuRuCl_8$ (**2**)	[0, 0]	9.97	Triclinic, $P\bar{1}$	a^-b^-c	1.55
$(PPDA)_2AgRuBr_8$ (**3**)	[0, 0]	10.26	Triclinic, $P\bar{1}$	a^-b^-c	1.67
$(PPDA)_2AgMoCl_8$ (**4**)	[0, 0]	10.19	Triclinic, $P\bar{1}$	a^-b^-c	2.05
$(1,4\text{-}BDA)_2AgRuCl_8$ (**5**)	[0, 0]	10.40	Monoclinic, $C2/m$	$a^0b^-c^0$	1.89
$(1,4\text{-}BDA)_2AgRuBr_8$ (**6**)	[0, 0]	9.35	Triclinic, $P\bar{1}$	a^-b^-c	1.60
$(1,3\text{-}PDA)_2AgRuCl_8$ (**7**) 300 K	[½, 0]	9.11	Monoclinic, $C2/m$	$a^0b^-c^0$	1.86
$(1,3\text{-}PDA)_2AgRuCl_8$ (**7**) 220 K	[½, 0]	8.64	Monoclinic, $C2/m$	$a^-a^-c^0/a^-a^-c^0$	-
$(1,3\text{-}PDA)_2AgRuBr_8$ (**8**)	[½, 0]	8.82	Monoclinic, $C2/m$	$a^-a^-c^0/a^-a^-c^0$	1.70

Figure 2a and b shows the crystal structure of **1** as a representative example of the $(PPDA)_2M^IM^{III}X_8$ series (**1** – **4**). It has alternating $[AgCl_6]$ and $[RuCl_6]$ polyhedra in the perovskite layer and PPDA between the layers. The $[AgCl_6]$ polyhedra exhibit shorter Ag-Cl_{ax} bonds (2.439 Å) than the Ag-Cl_{eq} bonds (2.943 Å and 2.945 Å) (Table S3). The $[RuCl_6]$ octahedra exhibit Ru-Cl bond lengths of 2.357 Å, 2.367 Å and 2.369 Å, of which the shortest and longest bonds are at the equatorial positions. Its elemental composition as well as the Ag^I and Ru^{III} oxidation states have been further confirmed by X-ray photoelectron spectroscopy (XPS) (Figure 2c, Figure S1-S3). The signs of higher oxidation states of Cu and Mo in the XPS spectra of **2** and **4** are likely due to surface oxidation. The SEM image of **1** shows a layer-by-layer morphology and crystal sizes in the micron range (Figure 2d). In the Cu^I analogue, **2**, the $[CuCl_6]$ polyhedral are more distorted with much shorter Cu-Cl_{ax} bonds than the Ag-Cl_{ax} in **1**, while the equatorial bonds are comparable with those of **1**. Compound **2** is a rare example of a stable and fully ordered Cu^I based layered double perovskite chloride. The ordered Cu^I-In^{III} compounds, (BA or PEA)$_4$CuInCl$_8$ (BA = butylammonium;[22] PEA = phenethylammonium[23]) have been reported recently.

In the case of **3**, the in-plane separation between Ag and Ru metals increases due to larger size of Br compared with Cl, while the interlayer gap changes marginally because of the comparable Ag-Br_{ax} and Ag-Cl_{ax} bond lengths. Although, the Mo-Cl_{eq} lengths in **4** are longer than the corresponding Ru-Cl lengths in **1** and **2**, the in-plane Ag to Mo separation is comparable due to an increase in the in-plane octahedral tilting. Between the $M^IM^{III}X_8$ layers of compounds **1**-**4**, PPDA forms a herringbone pattern through C-H···π interactions; these are weaker in the bromide analogue. The -NH_3^+ groups exhibit N(H)···X hydrogen bonding interactions with the equatorial and axial halides, some of which are quite strong (< 3.50 Å) (Table S4).[24] The shortest N···Cl distance of 3.0 Å is found in **4**, due to which the Ag^I-Cl-Mo^{III} angle is more twisted than in the other analogues (Figures S5-S9).

Figure 2e-h shows the structures of the Ag-Ru HLDP chlorides and bromides, **5** – **8**. These compounds show smaller twisting within the layers compared to the PPDA analogues (Figures S10-13), likely due to the flexibility of 1,4-BDA and 1,3-PDA. The 1,4-BDA spacer adopts an *anti* conformation in **5** (Figure S14). This conformation is typically found in layered perovskites at higher temperature,[25,26] while the *gauche* conformation often forms at room temperatures.[4,27–29] Notably, in the bromide compound **6**, 1,4-BDA exhibits two crystallographically unique cations in the *gauche* conformation. The 1,3-PDA spacer is present in the *anti* conformation, in the chloride **7**, while a mixed *anti* and *eclipsed* conformation (Figure S14) is found in the bromide analogue **8**. Interestingly, **7** shows a phase transition accompanied by a conformational change to the *anti* and *eclipsed* forms of 1,3-PDA on cooling to 220 K (Figure S15). The 220 K phase shows no changes in either the space group or the layer stacking pattern, but the interlayer separation decreases from 9.11 Å to 8.64 Å and the structure resembles the bromide

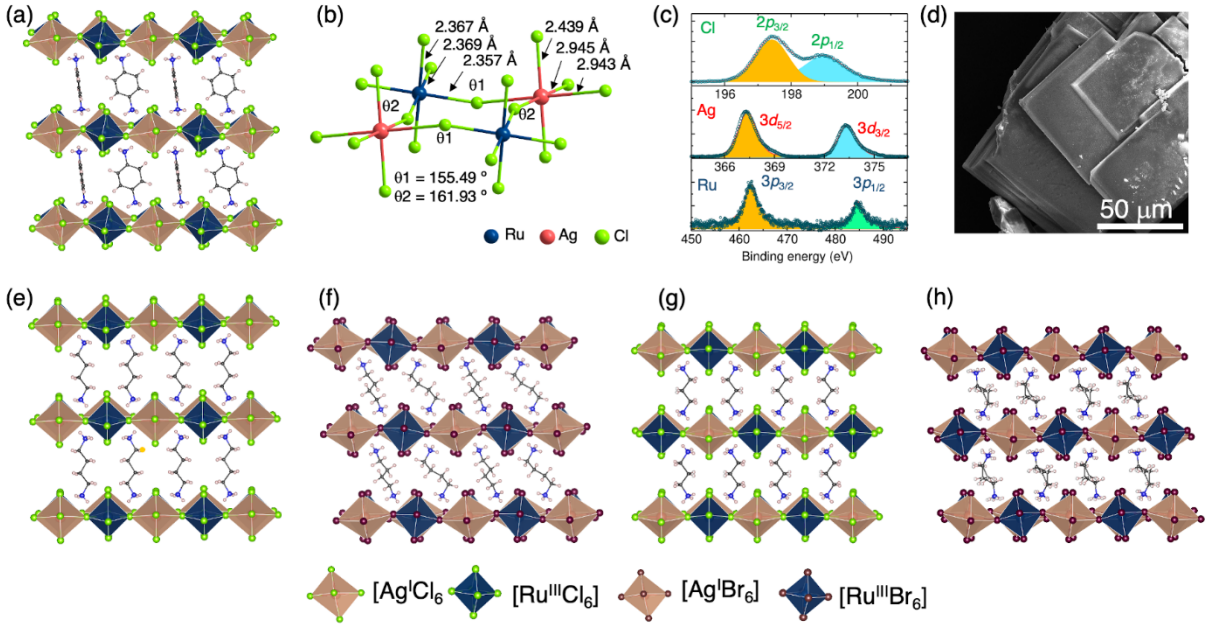

Figure 2. (a) Single-crystal X-ray structure of **1**. (b) Ball and stick model of **1** showing the bond lengths and in-plane connectivity of $[AgCl_6]$ and $[RuCl_6]$ octahedra. The M^I-X-M^{III} bond angles are also given. (c) Core level Ru (3*p*), Ag (3*d*) and Cl (2*p*) XP spectra of **1**. (d) SEM image of **1**. (e) - (h) Single-crystal X-ray structures of (e) **5**, (f) **6**, (g) **7** and (h) **8**.

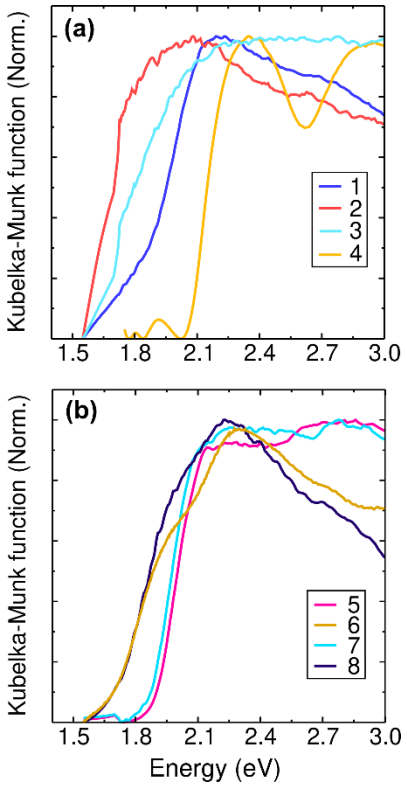

Figure 3. UV-visible absorption of HLDP halides. (a) Spectra of **1**– **4**; (b) Spectra of **5** – **8**.

analogue **8**. In the 220 K phase, the $[AgCl_6]$ and $[RuCl_6]$ octahedra are axially compressed and equatorially expanded compared to the 300 K phase and these changes are more significant for $[AgCl_6]$. It seems that the stacking pattern in **1** – **8** is dependent on the alkyl chain length – the 4C chains of PPDA and 1,4-BDA form [0, 0] phases, while the 3C chain 1,3-PDA forms [½, 0] phases (Figure 1, see above); this is consistent with most previous reports on related compounds (Table S1). We have adopted a Glazer-like notation to describe the octahedral tilt systems in these compounds (Table 1).[30]

The band gaps of **1** – **4** lie in the range 1.55 - 2.05 eV (Figure 3a), which is comparable to some of the Bi^{III} HLDP iodides.[7] Compound **1** shows a wider band gap than **2** and **3**, but it is narrower than **4**. The narrow band gap of **2** compared to **1** is consistent with Cu^IBi^{III} and Ag^IBi^{III} HLDP iodides reported elsewhere.[7] Because of the lower electronegativity of Br than Cl, the band gap of **3** is smaller than **1**. In addition to size and electronegativity, the M^I-X-M^{III} angles also influence the band gap. Specifically, deviations of the M^I-X-M^{III} angles from 180° lead to a decrease in the M-X orbital overlap, thereby increasing the band gap.[31] Compounds **5** – **8** with flexible spacers show band gaps comparable to the analogous PPDA perovskites (Figure 3b), suggesting that the organic spacers barely influence the electronic transitions. Earlier reports suggest that Pb-based hybrid layered perovskite iodides[32–34] and bromides[35,36] show slight band gap increases with increasing spacer length. We also note that the d-d transitions can be seen at 1.91, 2.31 and 2.90 eV in **4**, in agreement with previous work on K_3MoCl_6.[37] We did not observe any photoluminescent behavior. In future work, we shall be performing electronic structure calculations on this new family of compounds.

The magnetic susceptibilities of the compounds $(PPDA)_2Ag^IRu^{III}Cl_8$ (**1**) and $(PPDA)_2Ag^IMo^{III}Cl_8$ (**4**) were measured between 2 K and 300 K, as described in the Supplementary Information. These compounds feature widely separated Ru^{3+} and Mo^{3+} ions, of > 7.18 Å and > 7.31 Å, respectively, within the perovskite layers and are not expected to exhibit strong magnetic interactions. Note that the M^{III} to M^{III} distances between the layers are > 10 Å (Table 1). Taking the results for the $(PPDA)_2Ag^IMo^{III}Cl_8$ (**4**) first, the data show excellent agreement with the Curie-Weiss law (Figure 4a). The derived magnetic moment, $\mu_{eff} = 3.78\ \mu_B$, is in very good agreement with the expected value of 3.87 μ_B for a spin-only t_{2g}^3 Mo^{3+} ion. The value of the Curie-Weiss theta θ_{CW} = - 8.03 K, is indicative of weak antiferromagnetic coupling between the Mo^{III} ions. This is

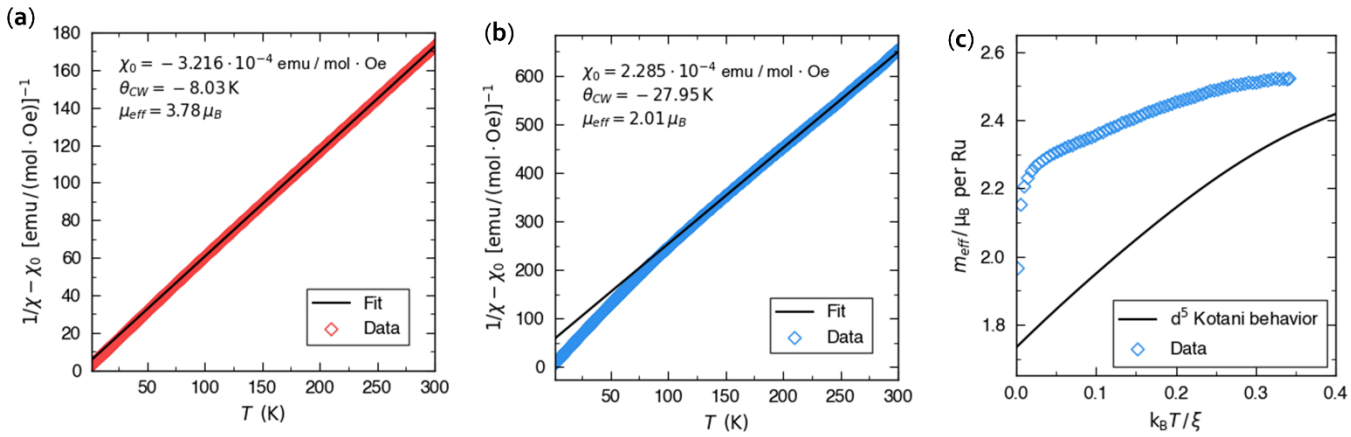

Figure 4. Magnetic data for the compounds $(PPDA)_2Ag^IMo^{III}Cl_8$ (**4**) and $(PPDA)_2Ag^IRu^{III}Cl_8$ (**1**). (a) Curie-Weiss fit for **4**; (b) Curie-Weiss fit for **1**; (c) Fitting of the magnetic moment data for **1** to the Kotani model with a spin-orbit coupling constant of 610 cm^{-1}.

consistent with the long superexchange pathway that passes via the d^{10} Ag^I ion, i.e. Mo-Cl-Ag-Cl-Mo. Compound **4** is a rare example of an extended magnetic solid based upon a Mo^{III} halide and our results show excellent agreement with the Curie-Weiss law. The molecular compounds, K_3MoCl_6 (μ_{eff} = 3.83 μ_β; θ_{CW} = -5 K),[38] appears to be the closest magnetic analog of compound **4**. We also note that while α-$MoCl_3$ forms a 2D honeycomb lattice, it is diamagnetic at and below room temperature due to the formation of Mo-Mo bonds with a distance of 2.76 Å.[39] The magnetic behaviour of $(PPDA)_2Ag^IRu^{III}Cl_8$ (**1**) is more complex due to the unquenched orbital angular momentum of the low spin t_{2g}^5 Ru^{III} ion. Fitting the high temperature data (150-300 K) to the Curie-Weiss law (Figure 4b) yields a moment, μ_{eff} of 2.01 μ_β and a θ_{CW} of –27.95 K. The larger θ_{CW} points to slightly stronger exchange coupling in **1** compared with **4**. If the variation of the magnetic moment with temperature is compared with the trend predicted by the Kotani theory for t_{2g}^5,[40] the fit is rather poor, irrespective of the choice of spin-orbit coupling constant (Figure 4c). The breakdown of the Kotani model for t_{2g}^5 is similar to our recent findings for other Ru^{III} compounds, e. g. $(CH_3NH_3)_2NaRuCl_6$.[25] There are several possible reasons for this, including deviations from perfect octahedral symmetry for Ru^{III} and breakdown of the assumption that the RuIII ions are non-interacting. However, the geometry of the $RuCl_6$ unit in **1** is almost perfectly octahedral and the Ru···Ru distances are long (Table S3). Thus, we do not believe that the discrepency can be explained on the basis of these two factors and it seems more likely that there is a need to revisit the Kotani theory for low-spin d^5 ions.

In conclusion, we have isolated and structurally characterized seven new hybrid layered perovskite halides of Ru^{III} and one of Mo^{III}. The results showcase that all the chemical components - including the organic diamine spacer, the monovalent metal, the trivalent metal and the halide - are tunable, thereby significantly expanding the compositional and structural diversity of the HLDP halides family. We hope that these findings will serve as guidance for future developments in TM-based double perovskites, both in terms new materials discoveries and applications.

ASSOCIATED CONTENT

Supporting Information

Synthesis and characterization, scXRD refinement details, key bond lengths and bond angles, hydrogen bond interactions, power x-ray diffraction patterns, x-ray photoelectron spectra (XPS), scanning electron microscope (SEM) images, additional single-crystal x-ray structures, octahedral tilting

Accession Codes

CCDC (2122532 – 2122540) contain the supplement crystallographic data for this paper which can be obtained free of charge via www.ccdc.cam.ac.uk/data_request/cif, by emailing at data_request@ccdc.cam.ac.uk, or by contacting the Cambridge Crystallographic Data Centre, 12 Union Road, Cambridge CB2 1EZ, UK; fax: +44 1223 336033

AUTHOR INFORMATION

Corresponding Authors

Ram Seshadri - *Materials Department and Materials Research Laboratory, University of California Santa Barbara, CA 93106, United States; ORCID: orcid.org/0000-0001-5858-4027; Email: seshadri@mrl.ucsb.edu*

Anthony K. Cheetham - *Materials Department and Materials Research Laboratory, University of California Santa Barbara, CA 93106, United States; Department of Materials Science & Engineering, National University of* Singapore*, 117576 Singapore; ORCID: orcid.org/0000-0003-1518-4845; Email: akc30@cam.ac.uk*

Notes

The authors declare no competing financial interests.

ACKNOWLEDGMENT

This work was supported by the Department of Energy, Office of Science, Basic Energy Sciences, under Grant No. SC0012541. PV thanks the Department of Science & Technology (DST) of Govt. of India for the Overseas Postdoctoral Visiting Fellowship (Award No. JNC/AO/A.0610-1(3)/2018-03), the Science & Engineering Research Board (SERB) of the Govt. of India for the Ramanujan Fellowship (Award No. RJF/2020/000106), and the Jawaharlal Nehru Centre for Advanced Scientific Research (JNCASR) Bangalore for the financial support and the research infrastructure. We acknowledge the shared facility of the Materials Research Science and Engineering Center (MRSEC) at the UC Santa Barbara under the National Science Foundation (NSF) grant number DMR 1720256. JLZ also acknowledges the support of the NSF Graduate Research Fellowship Program under Grant No. 1650114. AKC thanks the Ras al Khaimah Centre for Advanced Materials for financial support.

REFERENCES

(1) Smith, I. C.; Hoke, E. T.; Solis-Ibarra, D.; McGehee, M. D.; Karunadasa, H. I. A Layered Hybrid Perovskite Solar-Cell Absorber with Enhanced Moisture Stability. *Angew. Chem. Int. Ed.* **2014**, *53*, 11232–11235.

(2) Cao, D. H.; Stoumpos, C. C.; Farha, O. K.; Hupp, J. T.; Kanatzidis, M. G. 2D Homologous Perovskites as Light-Absorbing Materials for Solar Cell Applications. *J. Am. Chem. Soc.* **2015**, *137*, 7843–7850.

(3) Evans, H. A.; Mao, L.; Seshadri, R.; Cheetham, A. K. Layered Double Perovskites. *Annu. Rev. Mater. Res.* **2021**, *51*, 351–380.

(4) Mao, L.; Teicher, S. M. L.; Stoumpos, C. C.; Kennard, R. M.; DeCrescent, R. A.; Wu, G.; Schuller, J. A.; Chabinyc, M. L.; Cheetham, A. K.; Seshadri, R. Chemical and Structural Diversity of Hybrid Layered Double Perovskite Halides. *J. Am. Chem. Soc.* **2019**, *141*, 19099–19109.

(5) Jana, M. K.; Janke, S. M.; Dirkes, D. J.; Dovletgeldi, S.; Liu, C.; Qin, X.; Gundogdu, K.; You, W.; Blum, V.; Mitzi, D. B. Direct-Bandgap 2D Silver–Bismuth Iodide Double Perovskite: The Structure-Directing Influence of an Oligothiophene Spacer Cation. *J. Am. Chem. Soc.* **2019**, *141*, 7955–7964.

(6) Lassoued, M. S.; Bi, L.-Y.; Wu, Z.; Zhou, G.; Zheng, Y.-Z. Piperidine-Induced Switching of the Direct Band Gaps of Ag(I)/Bi(III) Bimetallic Iodide Double Perovskites. *J. Mater. Chem. C* **2020**, *8*, 5349–5354.

(7) Bi, L.-Y.; Hu, Y.-Q.; Li, M.-Q.; Hu, T.-L.; Zhang, H.-L.; Yin, X.-T.; Que, W.-X.; Lassoued, M. S.; Zheng, Y.-Z. Two-Dimensional Lead-Free Iodide-Based Hybrid Double Perovskites: Crystal Growth, Thin-Film Preparation and Photocurrent Responses. *J. Mater. Chem. A* **2019**, *7*, 19662–19667.

(8) Bi, L.-Y.; Hu, T.-L.; Li, M.-Q.; Ling, B.-K.; Lassoued, M. S.; Hu, Y.-Q.; Wu, Z.; Zhou, G.; Zheng, Y.-Z. Template Effects in Cu(I)–Bi(III) Iodide Double Perovskites: A Study of Crystal Structure, Film Orientation, Band Gap and Photocurrent Response. *J. Mater. Chem. A* **2020**, *8*, 7288–7296.

(9) Fu, D.; Wu, S.; Liu, Y.; Yao, Y.; He, Y.; Zhang, X.-M. A Lead-Free Layered Dion–Jacobson Hybrid Double Perovskite Constructed by an Aromatic Diammonium Cation. *Inorg. Chem. Front.* **2021**, *8*, 3576–3580.

(10) Li, X.; Traoré, B.; Kepenekian, M.; Li, L.; Stoumpos, C. C.; Guo, P.; Even, J.; Katan, C.; Kanatzidis, M. G. Bismuth/Silver-Based Two-Dimensional Iodide Double and One-Dimensional Bi Perovskites: Interplay between Structural and Electronic Dimensions. *Chem. Mater.* **2021**, *33*, 6206–6216.

(11) Ruan, H.; Guo, Z.; Lin, J.; Liu, K.; Guo, L.; Chen, X.; Zhao, J.; Liu, Q.; Yuan, W. Structure and Optical Properties of Hybrid-Layered-Double Perovskites $(C_8H_{20}N_2)_2AgMBr_8$ (M = In, Sb, and Bi). *Inorg. Chem.* **2021,** *60*, 14629–14635.

(12) Han, C.; Bradford, A. J.; Slawin, A. M. Z.; Bode, B. E.; Fusco, E.; Lee, S. L.; Tang, C. C.; Lightfoot, P. Structural Features in Some Layered Hybrid Copper Chloride Perovskites: $ACuCl_4$ or A_2CuCl_4. *Inorg. Chem.* **2021**, *60*, 11014–11024.

(13) Gregson, A. K.; Day, P.; Leech, D. H.; Fair, M. J.; Gardner, W. E. Magnetic Susceptibility and Magnetization of the Ionic Ferromagnets Dipotassium, Dirubidium, and Dicaesium Tetrachlorochromate(II). *J. Chem. Soc. Dalt. Trans.* **1975**, 1306–1311.

(14) Nakayama, Y.; Nishihara, S.; Inoue, K.; Suzuki, T.; Kurmoo, M. Coupling of Magnetic and Elastic Domains in the Organic–Inorganic Layered Perovskite-Like $(C_6H_5C_2H_4NH_3)_2Fe^{II}Cl_4$ Crystal. *Angew. Chem. Int. Ed.* **2017**, *56*, 9367–9370.

(15) Polyakov, A. O.; Arkenbout, A. H.; Baas, J.; Blake, G. R.; Meetsma, A.; Caretta, A.; van Loosdrecht, P. H. M.; Palstra, T. T. M. Coexisting Ferromagnetic and Ferroelectric Order in a $CuCl_4$-Based Organic–Inorganic Hybrid. *Chem. Mater.* **2012**, *24*, 133–139.

(16) Jaffe, A.; Mack, S. A.; Lin, Y.; Mao, W. L.; Neaton, J. B.; Karunadasa, H. I. High Compression-Induced Conductivity in a Layered Cu–Br Perovskite. *Angew. Chem. Int. Ed.* **2020**, *59*, 4017–4022.

(17) Castro-Castro, L. M.; Guloy, A. M. Organic-Based Layered Perovskites of Mixed-Valent Gold(I)/Gold(III) Iodides. *Angew. Chem. Int. Ed.* **2003**, *42*, 2771–2774.

(18) Vishnoi, P.; Seshadri, R.; Cheetham, A. K. Why Are Double Perovskite Iodides so Rare?. *J. Phys. Chem. C* **2021**, *125*, 11756–11764.

(19) Banerjee, A.; Bridges, C. A.; Yan, J.-Q.; Aczel, A. A.; Li, L.; Stone, M. B.; Granroth, G. E.; Lumsden, M. D.; Yiu, Y.; Knolle, J.; Bhattacharjee, S.; Kovrizhin, D. L.; Moessner, R.; Tennant, D. A.; Mandrus, D. G.; Nagler, S. E. Proximate Kitaev Quantum Spin Liquid Behaviour in a Honeycomb Magnet. *Nat. Mater.* **2016**, *15*, 733–740.

(20) Vishnoi, P.; Zuo, J. L.; Strom, T. A.; Wu, G.; Wilson, S. D.; Seshadri, R.; Cheetham, A. K. Structural Diversity and Magnetic Properties of Hybrid Ruthenium Halide Perovskites and Related Compounds. *Angew. Chem. Int. Ed.* **2020**, *59*, 8974–8981.

(21) Vishnoi, P.; Zuo, J. L.; Cooley, J. A.; Kautzsch, L.; Gómez-Torres, A.; Murillo, J.; Fortier, S.; Wilson, S. D.; Seshadri, R.; Cheetham, A. K. Chemical Control of Spin-Orbit Coupling and Charge Transfer in Vacancy-Ordered Ruthenium(IV) Halide Perovskites. *Angew. Chem. Int. Ed.* **2021**, *60*, 5184–5188.

(22) Connor, B. A.; Smaha, R. W.; Li, J.; Gold-Parker, A.; Heyer, A. J.; Toney, M. F.; Lee, Y. S.; Karunadasa, H. I. Alloying a Single and a Double Perovskite: A $Cu^+/2^+$ Mixed-Valence Layered Halide Perovskite with Strong Optical Absorption. *Chem. Sci.* **2021**, *12*, 8689–8697.

(23) Aubrey, M. L.; Saldivar Valdes, A.; Filip, M. R.; Connor, B. A.; Lindquist, K. P.; Neaton, J. B.; Karunadasa, H. I. Directed Assembly of Layered Perovskite Heterostructures as Single Crystals. *Nature* **2021**, *597*, 355–359.

(24) Steiner, T. Hydrogen-Bond Distances to Halide Ions in Organic and Organometallic Crystal Structures: Up-to-Date Database Study. *Acta Crystallogr. Sect. B* **1998**, *54*, 456–463..

(25) Courseille, C.; Chanh, N. B.; Maris, T.; Daoud, A.; Abid, Y.; Laguerre, M. Crystal Structure and Phase Transition in the Perovskite-Type Layer Molecular Composite $NH_3(CH_2)_4NH_3PbCl_4$. *Phys. status solidi* **1994**, *143*, 203–214.

(26) Maris, T.; Bravic, G.; Chanh, N. B.; Leger, J. M.; Bissey, J. C.; Villesuzanne, A.; Zouari, R.; Daoud, A. Structures and Thermal Behavior in the Series of Two-Dimensional Molecular Composites NH_3-$(CH_2)_4$-NH_3MCl_4 Related to the Nature of the Metal M. Part 1: Crystal Structures and Phase Transitions in the Case *M* = Cu and Pd. *J. Phys. Chem. Solids* **1996**, *57*, 1963–1975.

(27) Han, Y.; Li, Y.; Wang, Y.; Cao, G.; Yue, S.; Zhang, L.; Cui, B.-B.; Chen, Q. From Distortion to Disconnection: Linear Alkyl Diammonium Cations Tune Structure and Photoluminescence of Lead Bromide Perovskites. *Adv. Opt. Mater.* **2020**, *8*, 1902051.

(28) Amami, M.; Zouari, R.; Ben Salah, A.; Burzlaff, H. 1,4-Butanediammonium Tetrachloromercurate(II). *Acta Crystallogr. Sect. E* **2002**, *58*, m357-m359.

(29) Shen, Y.; Liu, Y.; Ye, H.; Zheng, Y.; Wei, Q.; Xia, Y.; Chen, Y.; Zhao, K.; Huang, W.; Liu, S. (Frank). Centimeter-Sized Single Crystal of Two-Dimensional Halide Perovskites Incorporating Straight-Chain Symmetric Diammonium Ion for X-Ray Detection. *Angew. Chem. Int. Ed.* **2020**, *59* 14896–14902.

(30) McNulty, J. A.; Lightfoot, P. Structural Chemistry of Layered Lead Halide Perovskites Containing Single Octahedral Layers. *IUCrJ* **2021**, *8*, 485–513.

(31) Vasileiadou, E. S.; Hadar, I.; Kepenekian, M.; Even, J.; Tu, Q.; Malliakas, C. D.; Friedrich, D.; Spanopoulos, I.; Hoffman, J. M.; Dravid, V. P.; Kanatzidis, M. G. Shedding Light on the Stability and Structure–Property Relationships of Two-Dimensional Hybrid Lead Bromide Perovskites. *Chem. Mater.* **2021**, *33*, 5085–5107.

(32) Safdari, M.; Svensson, P. H.; Hoang, M. T.; Oh, I.; Kloo, L.; Gardner, J. M. Layered 2D Alkyldiammonium Lead Iodide Perovskites: Synthesis, Characterization, and Use in Solar Cells. *J. Mater. Chem. A* **2016**, *4*, 15638–15646.

(33) Phuyal, D.; Safdari, M.; Pazoki, M.; Liu, P.; Philippe, B.; Kvashnina, K. O.; Karis, O.; Butorin, S. M.; Rensmo, H.; Edvinsson, T.; Kloo, L.; Gardner, J. M. Electronic Structure of Two-Dimensional Lead(II) Iodide Perovskites: An Experimental and Theoretical Study. *Chem. Mater.* **2018**, *30*, 4959–4967.

(34) Ma, C.; Shen, D.; Ng, T.-W.; Lo, M.-F.; Lee, C.-S. 2D Perovskites with Short Interlayer Distance for High-Performance Solar Cell Application. *Adv. Mater.* **2018**, *30*, 1800710.

(35) Kitazawa, N.; Aono, M.; Watanabe, Y. Excitons in Organic–Inorganic Hybrid Compounds $(C_nH_{2n+1}NH_3)_2PbBr_4$ (n = 4, 5, 7 and 12). *Thin Solid Films* **2010**, *518*, 3199–3203.

(36) Deng, C.; Zhou, G.; Chen, D.; Zhao, J.; Wang, Y.; Liu, Q. Broadband Photoluminescence in 2D Organic–Inorganic Hybrid Perovskites: $(C_7H_{18}N_2)PbBr_4$ and $(C_9H_{22}N_2)PbBr_4$. *J. Phys. Chem. Lett.* **2020**, *11*, 2934–2940..

(37) Kamalov, R. V; Volkovich, V. A.; Polovov, I. B.; Vasin, B. D. Stability of Complex Molybdenum(III) Ions in Molten Alkali Metal Chlorides. *Russ. Metall.* **2012**, *2012*, 114–118.

(38) Van Dalen, P. A.; Steenland, M. J. Susceptibility Study of the Magnetic State of K_3MoCl_6. *Physica* **1967**, *36*, 275–288.

(39) McGuire, M. A.; Yan, J.; Lampen-Kelley, P.; May, A. F.; Cooper, V. R.; Lindsay, L.; Puretzky, A.; Liang, L.; KC, S.; Cakmak, E.; Calder, S.;

$LiScMo_3O_8$

Sales, B. C. High-Temperature Magnetostructural Transition in van Der Waals-Layered α-$MoCl_3$. *Phys. Rev. Mater.* **2017**, *1*, 64001.

(40) Kotani, M. On the Magnetic Moment of Complex Ions. (I). *J. Phys. Soc. Japan* **1949**, *4*, 293–297.

Insert Table of Contents artwork here

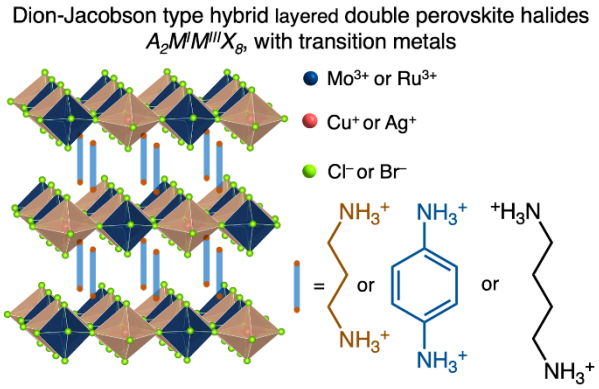

Supporting Information

Hybrid Layered Double Perovskite Halides of Transition Metals

Pratap Vishnoi[a,b], Julia L. Zuo[a], Xiaotong Li[c], Devesh Chandra Binwal[b], Kira E. Wyckoff[a], Lingling Mao [a,d], Linus Kautzsch[a], Guang Wu[e], Stephen D. Wilson[a], Mercouri G. Kanatzidis[c], Ram Seshadri,[a]* Anthony K. Cheetham[a,f]*

[a]Materials Department and Materials Research Laboratory, University of California Santa Barbara, California 93106, United States

[b]New Chemistry Unit and International Centre for Materials Science, Jawaharlal Nehru Centre for Advanced Scientific Research (JNCASR), Jakkur P.O., Bangalore 560064, India

[c]Department of Chemistry, Northwestern University, Evanston, Illinois 60208, United States

[d]Department of Chemistry, Southern University of Science and Technology (SUSTech), Shenzhen, 518055 China

[e]Department of Chemistry and Biochemistry, University of California, Santa Barbara, California 93106, United States

[f]Department of Materials Science & Engineering, National University of Singapore, 117576 Singapore, Singapore

Content

EXPERIMENTAL SECTION

Materials. The starting materials, anhydrous $RuCl_3$ (Strem Chemicals), $MoCl_3$ (Strem Chemicals), AgCl (Sigma Aldrich), 1,2-ethanediamine (Sigma Aldrich), 1,3-propanediamine (Sigma Aldrich), 1,4-butanediamine (Sigma Aldrich), *para*-phenylenediamine (Sigma Aldrich), 1,1'-biphenyl-4,4'-diamine (Sigma Aldrich), 50 wt.% H_3PO_2 in H_2O (Sigma Aldrich), 37 wt.% HCl in H_2O (Merck) and 48 wt. % HBr in H_2O (Sigma Aldrich) were purchased commercially and used with no further purification. All the compounds were synthesized as single crystals under the hydrothermal conditions.

Synthesis of $(PPDA)_2AgRuCl_8$ (1). *para*-Phenylenediamine (108.15 mg, 1.0 mmol), AgCl (71.65 mg, 0.5 mmol), $RuCl_3$ (103.70 mg, 0.5 mmol), 37 wt.% aqueous HCl (2.0 mL) and 50 wt.% aqueous H_3PO_2 (66 mg, ~ 66 µL, 0.5 mmol) were taken in a 23 mL Teflon vial. The Teflon vial containing the reaction mixture was closed in a stainless-steel autoclave, and heated in a furnace at 160 °C for 48 h. The autoclave was cooled to room temperature to obtain red crystals of **1**. The crystals were filtered out of the acid mother liquor, washed with copious amounts water followed by ethanol, and dried in vacuum oven at 60 °C. Yield 160 mg; 45% based on Ru.

Synthesis of $(PPDA)_2CuRuCl_8$ (2). *para*-Phenylenediamine (108.15 mg, 1.0 mmol), CuCl (49.50 mg, 0.5 mmol), $RuCl_3$ (103.70 mg, 0.5 mmol), 37 wt.% aqueous HCl (2.0 mL) and 50 wt.% aqueous H_3PO_2 (66 mg, ~ 66 µL, 0.5 mmol) were taken in a 23 mL Teflon vial. The Teflon vial containing the reaction mixture was closed in a stainless-steel autoclave, and heated in a furnace at 160 °C for 48 h. The autoclave was cooled to room temperature to obtain black crystals of **2**. The crystals were filtered out of the acid mother liquor, washed with water and ethanol, and dried in vacuum at 60 °C. Yield 123 mg; 37% based on Ru.

Synthesis of $(PPDA)_2AgRuBr_8$ (3). *para*-Phenylenediamine (108.15 mg, 1.0 mmol), AgCl (71.65 mg, 0.5 mmol), $RuCl_3$ (103.70 mg, 0.5 mmol), 48 wt.% aqueous HBr (2.0 mL) and 50 wt.% aqueous H_3PO_2 (66 mg, ~ 66 µL, 0.5 mmol) were taken in a 23 mL Teflon vial. The Teflon vial containing the reaction mixture was closed in a stainless-steel autoclave, and heated in a furnace at 160 °C for 48 h. The autoclave was cooled to room temperature to dark red crystals of **3**. The crystals were filtered out of the acid mother liquor, washed with water and ethanol, and dried in vacuum at 60 °C. Yield 320 mg; 60% based on Ru.

Synthesis of $(PPDA)_2AgMoCl_8$ (4). *para*-Phenylenediamine (108.15 mg, 1.0 mmol), AgCl (71.65 mg, 0.5 mmol), $MoCl_3$ (101.5 mg, 0.5 mmol), 37 wt.% aqueous HCl (2.0 mL) and 50 wt.% aqueous

H_3PO_2 (66 mg, ~ 66 µL, 0.5 mmol) were taken in a 23 mL Teflon vial. The Teflon vial containing the reaction mixture was closed in a stainless-steel autoclave, and heated in a furnace at 160 °C for 48 h. The autoclave was cooled to room temperature to obtain red crystals of **4**. The crystals were filtered out of the acid mother liquor, washed with ethanol and dried in vacuum at 60 °C. The colorless crystals of impurity were separated manually under optical microscope. Yield 250 mg; 71% based on Mo.

Synthesis of (1,4-BDA)$_2$AgRuCl$_8$ (5). 1,4-Butanediamine (88.15 mg, 1.0 mmol), AgCl (71.65 mg, 0.5 mmol), $RuCl_3$ (103.70 mg, 0.5 mmol), 37 wt.% aqueous HCl (2.0 mL) and 50 wt.% aqueous H_3PO_2 (66 mg, ~ 66 µL, 0.5 mmol) were taken in a 23 mL Teflon vial. The Teflon vial containing the reaction mixture was closed in a stainless-steel autoclave, and heated in a furnace at 160 °C for 48 h. The autoclave was cooled to room temperature to obtain dark red crystals of **5**. The crystals were filtered out of the acid mother liquor, washed with water and ethanol, and dried in vacuum at 60 °C. Yield 195 mg; 58 % based on Ru.

Synthesis of (1,4-BDA)$_2$AgRuBr$_8$ (6). 1,4-Butanediamine (88.15 mg, 1.0 mmol), AgCl (71.65 mg, 0.5 mmol), $RuCl_3$ (103.70 mg, 0.5 mmol), 48 wt.% aqueous HBr (2.0 mL) and 50 wt.% aqueous H_3PO_2 (66 mg, ~ 66 µL, 0.5 mmol) were taken in a 23 mL Teflon vial. The Teflon vial containing the reaction mixture was closed in a stainless-steel autoclave, and heated in a furnace at 160 °C for 48 h. The autoclave was cooled to room temperature to obtain black compound which was filtered out from the acid mother liquor, washed with water and ethanol, and dried in vacuum at 60 °C. The product was a mixture of the compound **6** and unknown impurities: the shiny black and long crystals of **6** were separated under optical microscope. Yield 103 mg; 20% based on Ru.

Synthesis of (1,3-PDA)$_2$AgRuCl$_8$ (7). 1,3-Propanediamine (74.10 mg, 1.0 mmol), AgCl (71.65 mg, 0.5 mmol), $RuCl_3$ (103.70 mg, 0.5 mmol), 37 wt.% aqueous HCl (2.0 mL) and 50 wt.% aqueous H_3PO_2 (66 mg, ~ 66 µL, 0.5 mmol) were taken in a 23 mL Teflon vial. The Teflon vial containing the reaction mixture was closed in a stainless-steel autoclave, and heated in a furnace at 160 °C for 48 h. The autoclave was cooled to room temperature to obtain dark red crystals of **7**. The crystals were filtered out of the acid mother liquor, washed with water and ethanol, and dried in vacuum at 60 °C. Yield 175 mg; 54 % based on Ru.

Synthesis of (1,3-PDA)$_2$AgRuBr$_8$ (8). 1,3-Propanediamine (74.10 mg, 1.0 mmol), AgCl (71.65 mg, 0.5 mmol), $RuCl_3$ (103.70 mg, 0.5 mmol), 48 wt.% aqueous HBr (2.0 mL) and 50 wt.% aqueous H_3PO_2 (66 mg, ~ 66 µL, 0.5 mmol) were taken in a 23 mL Teflon vial. The Teflon vial

containing the reaction mixture was closed in a stainless-steel autoclave, and heated in a furnace at 160 °C for 48 h. The autoclave was cooled to room temperature to obtain dark red crystals of **8**. The crystals were filtered out of the acid mother liquor, washed with water and ethanol, and dried in vacuum at 60 °C. Yield 275 mg; 55% based on Ru.

Single crystal X-ray diffraction. The single-crystal X-ray diffraction data were collected on a Bruker Kappa ApexII diffractometer equipped with a *TRIUMPH* monochromator equipped with an APEXII CCD detector and Mo-Kα X-ray source (wavelength = 0.71073 Å) powered with 40 kV and 30 mA. The data collection was carried out in a ω-scan strategy. The data collection, integration and structure solutions were carried out on ApexII software. The crystals were held at room temperature throughout the data collection. Absorption corrections were made by using *SADABS*. *XPREP* was used for the indications of space group and look for the possibility of high symmetry space groups. The structures were solved by direct methods and refined by full-matrix least-squares on F^2 by using the *SHELXL-2014*.[S1] The non-hydrogen atoms were refined anisotropically. The hydrogen atoms of the organic spacers were placed in their geometrically idealized positions and refined with isotopic parameters as riding atoms. The X-ray pictures were drawn by using the VESTA 3.4.7.[S2]

The low-temperature structure of (1,3-PDA)$_2$AgRuCl$_8$ (**7**) were collected by cooling the crystals by continuous flow of liquid nitrogen. The crystals were gradually cooled to observe the change in the diffraction pattern and cell parameters. After the phase transitions occur, full data were collected at 220 K and the structure was solved and refined.

Powder X-ray diffraction. The phase purity of all the samples was examined by the powder x-ray diffraction (PXRD) data. The data were collected on a Panalytical Empyrean diffractometer equipped with a Cu-Kα x-ray source of wavelength 1.54056 Å. The simulated powder patterns were calculated from the crystallographic information files (CIFs) using the VESTA 3.4.7 software. The Le Bail refinement of the PXRD patterns were carried out by using GSAS-II software.[S3] The experimental diffractograms fit well to the simulated ones from scXRD data and the unit cell constants obtained from the scXRD data match closely with those extracted from the Le Bail fittings. The cell parameters are compared in the **Table S7**. The PXRD patterns are given in the **Figures S16-S23**.

X-ray photoelectron spectroscopy (XPS). The chemical compositions and the chemical environments of compounds **1**-**4** was further ascertained with the help of X-ray photoelectron spectroscopy (XPS). The XPS samples were prepared by grinding crystals of each sample into fine

powder. These powder samples were gently pressed onto an XPS sample holder using double-sided carbon tape. Measurements for the samples **1**-**3** were performed using a Thermo Fisher Escalab Xi+ XPS equipped with a monochromatic Al anode (photon energy = 1486.7 eV). The measurements for the sample **4** were performed on a PHI 5000 Versa Probe III instrument of ULVAC-PHI Inc. The survey scans were measured at 100 eV pass energy and the core-levels scans were carried out at 20 eV pass energy. All spectra were referenced to adventitious carbon at 284.8 eV. The data were fitted using the Fityk software with appropriate spin-orbit splitting and peak area ratios, and plotted using the Grace-5.1.22 software.

Figure S1 shows the wide range X-ray photoelectron survey spectra, showing the signals due to the elements that are present in the compounds with additional O surface contamination. **Figure S2** shows the core level spectra of M^{I} metals, M^{III} metals and *X* halides, and additional core level spectra are provided in the **Figure S3**. As expected, we detected signals for all the elements with required oxidation states (**Table S6**). In the case of **3**, contamination of Mo^{IV} and Mo^{V} has also been discovered along with the desired Mo^{III} state. The oxidation may have occurred while handling the sample in open atmosphere. The spectrum does not suggest reduction of Ag^{I} to Ag^{0} and therefore, we believe that the layer structure is intact, and the oxidized materials may not be a part of the perovskite layer.

Scanning electron microscopy (SEM). The scanning electron microscopic images were collected on a ThermoFischer Apreo C FEG SEM, fitted with an Everhart-Thornley Detector (ETD) for the detection of the secondary electrons. An acceleration voltage of 15 kV and an acceleration current of 0.10 nA were used. The SEM images of the layered doubler perovskites show layer-by-layer condensed structures and the crystallite size in microns (**Figure S4**).

Absorption spectroscopy. Optical diffuse reflectance measurements were performed using a Shimadzu UV-3600 UV–vis-NIR spectrometer operating in the 400 - 800 nm region using $BaSO_4$ as the reference for 100% reflectance. The band gaps of the materials were estimated by converting reflectance to absorption according to the Kubelka–Munk equation: $\alpha/S = (1 - R)^2(2R)^{-1}$, where *R* is the reflectance and α and *S* is the absorption and scattering coefficients, respectively.

Thermal studies. Thermogravimetric analysis (TGA) measurements for $(1,3\text{-PDA})_2AgRuCl_8$ (**7**) were carried out on a Discovery TGA instrument (TA Instruments). About 10 mg of the sample was taken in an aluminium crucible and heated in the temperature range of 50-1000 °C under a continuous flow of nitrogen gas (flow rate; 25 mL/minute) and the temperature ramp rate was kept at 10 °C min^{-1}. The Differential

scanning calorimeter (DSC) experiment was carried under liquid nitrogen flow on a DSC Q-2000 instrument from TA Inst. Co. in the temperature range of 100-450 K. The TGA curve is shown in the **Figure S15**.

Magnetic measurements. Magnetic susceptibility *versus* temperature measurements were performed on powdered samples mounted in plastic caps on a brass rod on a Quantum Design Magnetic Property Measurement System 3. Zero-field cooled (ZFC) and field cooled (FC) measurements were taken on warming from 2K to 300K under a constant field of 500Oe. We transformed the magnetic susceptibility χ versus temperature to an effective magnetic moment using the Curie law

$$m_{eff} = \sqrt{\frac{3k_B}{N_A \mu_B^2} \chi T}$$

where k_B is the Boltzmann constant, χ is the molar susceptibilities, T is the temperature, N_A is Avogadro's number and μ_B is Bohr magneton

Table S1. Reported DJ type $n = 1$ hybrid layered double perovskite halides.[a] For comparison, the compounds from this study are also included.

Compounds	**Diammonium cation spacer**	**Layer stacking pattern**	**Refs**
$(4AMP)_2AgBiI_8 \cdot 0.5H_2O$	4-aminomethylpiperidinium	[½, 0]	S4, S5
$(cis\text{-}1,4\text{-}CHDA)_2AgBiI_8.H_2O$	1,4-cyclohexanediammonium	[½, 0]	S6
$(1,3\text{-}CHDA)_2CuBiI_8$	1,3-cyclohexanediammonium	[½, 0]	S7
$(MPDA)_2CuBiI_8$	1-methylpiperidin-4-amine	[½, 0]	S7
$(3AMPY)_2AgBiI_8 \cdot H_2O$	3-(aminomethyl) pyridinium	[½, 0]	S5, S8
$(trans\text{-}1,4\text{-}CHDA)_2CuBiI_8.0.5H_2O$	1,4-cyclohexanediammonium	[0, 0]	S6
$(1,4\text{-}BDA)_2AgBiBr_8$	1,4-butanediammonium	[0, 0]	S9
$(C_8H_{20}N_2)_2AgInBr_8$	1,4-bis(methylammonium)cyclohexane	[0, 0]	S10
$(C_8H_{20}N_2)_2AgSbBr_8$	1,4-bis(methylammonium)cyclohexane	[0, 0]	S10
$(C_8H_{20}N_2)_2AgBiBr_8$	1,4-bis(methylammonium)cyclohexane	[0, 0]	S10
$(PPDA)_2AgRuCl_8$	*para*-phenylenediammonium	[0, 0]	This work
$(PPDA)_2CuRuCl_8$	*para*-phenylenediammonium	[0, 0]	This work
$(PPDA)_2AgMoCl_8$	*para*-phenylenediammonium	[0, 0]	This work
$(PPDA)_2AgRuBr_8$	*para*-phenylenediammonium	[0, 0]	This work
$(1,4\text{-}BDA)_2AgRuCl_8$	1,4-butanediammonium	[0, 0]	This work
$(1,4\text{-}BDA)_2AgRuBr_8$	1,4-butanediammonium	[0, 0]	This work
$(1,3\text{-}PDA)_2AgRuCl_8$ 300 K	1,3-propanediammonium	[½, 0]	This work
$(1,3\text{-}PDA)_2AgRuCl_8$ 220 K	1,3-propanediammonium	[½, 0]	This work
$(1,3\text{-}PDA)_2AgRuBr_8$	1,3-propanediammonium	[½, 0]	This work
$(AE_2T)_2AgBiI_8$	5,5′-diylbis(aminoethyl)-[2,2′-bithiophene	stacking fault	S11
$(OcDA)_2Au^IAu^{III}I_6 \cdot I_3$	Octane-1,8-diammonium	NA	S12
$(HpDA)_2Au^IAu^{III}I_6 \cdot I_3$	Heptane-1,7-diammonium	NA	S12

[a]The spacers with 4C or longer with even C chain give rise to [0, 0] stacked perovskites with the exception of first two compounds in this table [$(4AMP)_2AgBiI_8 \cdot 0.5H_2O$ and $(cis\text{-}1,4\text{-}CHDA)_2AgBiI_8.H_2O$], whereas the spacers with 3C chain give [½, 0] stacking.

Table S2. Single crystal x-ray data and structure refinement details of the hybrid layered double perovskite halides **1-8.**

	1	**2**	**3**
Empirical formula	$C_{12}H_{20}N_4AgRuCl_8$	$C_{12}H_{20}N_4CuRuCl_8$	$C_{12}H_{20}N_4AgRuBr_8$
Formula weight	712.86	668.53	1068.54
Temperature	300(2) K	298(2) K	300(2) K
Crystal system	Triclinic	Triclinic	Triclinic
Space group	*P*-1	*P*-1	*P*-1
Unit cell dimensions			
a	7.186(3) Å	7.160(2) Å	7.525(9) Å
b	7.561(3) Å	7.659(2) Å	7.919(10) Å
c	10.160(4) Å	9.972(3) Å	10.262(13) Å
α	90.703(11)°	91.307(8)°	91.12(3)°
β	93.266(11)°	92.633(10)°	92.55(3)°
γ	90.747(12)°	90.482(7)°	90.71(3)°
Volume	551.0(3) $Å^3$	546.1(3) $Å^3$	610.8(13) $Å^3$
Z	1	1	1
Density (calculated)	2.148 mg/m^3	2.033 mg/m^3	2.905 mg/m^3
Absorption coeff.	2.551 mm^{-1}	2.650 mm^{-1}	14.510 mm^{-1}
θ range for data collection	2.008 to 27.269 °	2.045 to 26.369°	1.987 to 24.994°
Reflections collected	4869	4935	3821
Data / restraints / parameters	2449 / 0 / 123	2227 / 0 / 123	2106 / 0 / 123
GoF on F^2	0.984	1.011	1.115
Final R indices [I>2sigma(I)]	R1 = 0.0427, wR2 = 0.0684	R1 = 0.0327, wR2 = 0.0551	R1 = 0.0986, wR2 = 0.2688
R indices (all data)	R1 = 0.0827, wR2 = 0.0796	R1 = 0.0537, wR2 = 0.0607	R1 = 0.1539, wR2 = 0.3026
	4	**5**	**6**
Empirical formula	$C_{12}H_{20}N_4AgMoCl_8$	$C_8H_{28}N_4AgRuCl_8$	$C_8H_{28}N_4AgRuBr_8$
Formula weight	707.73	672.88	1028.56
Temperature	298(2) K	300(2) K	300(2) K
Crystal system	Triclinic	Monoclinic	Triclinic
Space group	*P*-1	*C*2/m	*P*-1
Unit cell dimensions			
a	7.311(10) Å	10.465(3) Å	7.930(7) Å
b	7.583(7) Å	10.413(3) Å	7.949(7) Å
c	10.194(15) Å	10.424(3) Å	9.556(8) Å
α	91.12(3)°	90°	101.870(12)°
β	93.66(3)°	93.722(12)°	90.325(13)°
γ	90.96(5)°	90°	90.042(13)°
Volume	563.8(12) $Å^3$	1133.6(6) $Å^3$	589.5(9) $Å^3$
Z	1	2	1
Density (calculated)	2.084 mg/m^3	1.971 mg/m^3	2.897 mg/m^3
Absorption coeff.	2.379 mm^{-1}	2.472 mm^{-1}	15.028 mm^{-1}
θ range for data collection	2.002 to 26.370°	1.958 to 26.185 °	2.178 to 24.404°
Reflections collected	3964	1173	1834

Data / restraints / parameters	2257 / 0 / 123	1173 / 0 / 60	1834 / 0 / 99
GoF on F^2	1.007	1.082	1.043
Final R indices [I>2sigma(I)]	R1 = 0.0638, wR2 = 0.1634	R1 = 0.0682, wR2 = 0.1287	R1 = 0.0680, wR2 = 0.1593
R indices (all data)	R1 = 0.0842, wR2 = 0.1790	R1 = 0.1118, wR2 = 0.1425	R1 = 0.1429, wR2 = 0.1759
	7 at 300 K	**7 at 220 K**	**8**
Empirical formula	$C_6H_{24}N_4AgRuCl_8$	$C_6H_{24}N_4AgRuCl_8$	$C_6H_{24}N_4AgRuBr_8$
Formula weight	644.83	644.83	1000.51
Temperature	300(2) K	220(2) K	300(2) K
Crystal system	Monoclinic	Monoclinic	Monoclinic
Space group	*C*2/m	*C*2/m	*C*2/m
Unit cell dimensions			
a	10.492(5) Å	18.177(3) Å	18.569(6) Å
b	10.433(5) Å	7.1864(11) Å	7.519(3) Å
c	10.249(5) Å	7.8461(13) Å	8.168(3) Å
α	90°	90°	90°
β	117.257(11)°	107.545(3)°	108.113(7)°
γ	90°	90°	90°
Volume	997.3(8) $Å^3$	977.2(3) $Å^3$	1083.9(6) $Å^3$
Z	2	2	2
Density (calculated)	2.147 mg/m^3	2.191 mg/m^3	3.066 mg/m^3
Absorption coeff.	2.805 mm^{-1}	2.862 mm^{-1}	16.342 mm^{-1}
θ range for data collection	2.235 to 27.166°	2.350 to 26.253°	2.308 to 26.506°
Reflections collected	3761	1062	5685
Data / restraints / parameters	1172 / 0 / 56	1062 / 0 / 54	1212 / 55 / 83
GoF on F^2	1.054	1.128	1.109
Final R indices [I>2sigma(I)]	R1 = 0.0509, wR2 = 0.1191	R1 = 0.0586, wR2 = 0.677	R1 = 0.0467, wR2 = 0.1241
R indices (all data)	R1 = 0.0723, wR2 = 0.1287	R1 = 0.1213, wR2 = 0.0737	R1 = 0.0563, wR2 = 0.1292

Table S3. Key bond lengths (Å) and bond angles (°) in **1**-**8**.

$(PPDA)_2AgRuCl_8$ (**1**)	
bond lengths **axial bonds:** Ru1-Cl1 = 2.3672(15) Ag1-Cl2 = 2.4390(17) **equatorial bonds:** Ru1-Cl3 = 2.3572(14) Ru1-Cl4 = 2.3696(14) Ag1-Cl3 = 2.9434(16) Ag1-Cl4 = 2.9449(16)	**bond angles** **axial *cis* bonds:** Cl1-Ru1-Cl3, 89.83(5) & 90.17(5); Cl1-Ru1-Cl4, 88.56(5) & 91.44(5) Cl2-Ag1-Cl3, 84.03(5) & 95.97(5); Cl2-Ag1-Cl4, 88.95(5) & 91.05(5) **equatorial *cis* bonds:** Cl3-Ru1-Cl4 = 90.82(6) & 89.18(6) Cl3-Ag1-Cl4, 83.23(5) & 96.77(5) ***trans* bonds (axial & equatorial):** Cl1-Ru1-Cl1 = Cl3-Ru1-Cl3 = Cl4-Ru1-Cl4 = Cl2-Ag1-Cl2 = Cl3-Ag1-Cl3 = Cl4-Ag1-Cl4 = 180.0 **in-plane bridging bonds:** Ru1-Cl3-Ag1, 155.49(6); Ru1-Cl4-Ag1, 161.93(6) Averaged = 158.21
$(PPDA)_2CuRuCl_8$ (**2**)	
bond lengths **axial bonds:** Ru1-Cl1 = 2.3704(11) Cu1-Cl2 = 2.1775(11) **equatorial bonds:** Ru1-Cl3 = 2.3767(10) Ru1-Cl4 = 2.3656(10) Cu1-Cl3 = 2.9368(11) Cu1-Cl4 = 2.9469(11)	**bond angles** **axial *cis* bonds:** Cl1-Ru1-Cl3 = 88.81(4) & 91.19(4); Cl1- Ru1-Cl4 = 89.95(4) & 90.05(4) Cl2-Cu1-Cl3 = 89.08(4) & 90.92(4); Cl2-Cu1-Cl4 = 84.84(4) & 95.16(4) **equatorial *cis* bonds:** Cl3- Ru1-Cl4 = 88.81(4) & 91.19(4) Cl3-Cu1-Cl4 = 81.94(4) & 98.06(4) ***trans* bonds (axial & equatorial):** Cl1- Ru1-Cl1 = Cl3-Ru1-Cl3 = Cl4-Ru1-Cl4 = Cl2-Cu1-Cl2 = Cl3-Cu1-Cl3 = Cl4-Cu1-Cl4 = 180.0 **in-plane bridging bonds:** Ru1-Cl3-Cu1, 164.29(4); Ru1-Cl4-Cu1, 158.48(4) Averaged = 161.39
$(PPDA)_2AgRuBr_8$ (**3**)	
bond lengths **axial bonds:** Ru1-Br1 = 2.508(4) Ag1-Br2 = 2.542(4) **equatorial bonds:** Ru1-Br3 = 2.512(4) Ru1-Br4 = 2.500(4) Ag1-Br3 = 3.048(4) Ag1-Br4 = 3.051(4)	**bond angles** **axial *cis* bonds:** Br1-Ru1-Br3 = 88.93(11) & 91.07(11); Br1-Ru1-Br4 = 89.39(11) & 90.61(11) Br2-Ag1-Br3 = 87.46(11) & 92.54(11); Br2-Ag1-Br4 = 83.94(11) & 96.06(11) **equatorial *cis* bonds:** Br3-Ru1-Br4 = 89.33(14) & 90.67(14) Br3-Ag1-Br4 = 83.09(13) & 96.91(13) ***trans* bonds (axial & equatorial):** Br1-Ru1-Br1 = Br3-Ru1-Br3 = Br4-Ru1-Br4 = Br2-Ag1- Br2 = Br3-Ag1- Br3 = Br4-Ag1- Br4 = 180.0 **in-plane bridging bonds:** Ru1-Br3-Ag1, 162.53(); Ru1-Br4-Ag1, 155.77(13)

	Averaged = 159.15
$(PPDA)_2AgMoCl_8$ (**4**)	
bond lengths **axial bonds:** Mo1-Cl1 = 2.439(4) Ag1-Cl2 = 2.449(4) **equatorial bonds:** Mo1-Cl3 = 2.430(3) Mo1-Cl4 = 2.442(3) Ag1-Cl3 = 2.958(4) Ag1-Cl4 = 2.967(4)	**bond angles** **axial *cis* bonds:** Cl1-Mo1-Cl3 = 89.92(9) & 90.08(9); Cl1-Mo1-Cl4 = 88.61(9) & 91.39(9) Cl2-Ag1-Cl3 = 83.55(8) & 96.45(8); Cl2-Ag1-Cl4 = 88.64(8) & 91.36(8) **equatorial *cis* bonds:** Cl3-Mo1-Cl4, 89.68(12) and 90.32(12) Cl3-Ag1-Cl4, 84.06(11) and 95.94(11) ***trans* bonds (axial & equatorial):** Cl1-Mo1-Cl1 = Cl3-Mo1-Cl3 = Cl4-Mo1-Cl4 = Cl2-Ag1-Cl2 = Cl3-Ag1-Cl3 = Cl4-Ag1-Cl4 = 180.0 **in-plane bridging bonds:** Mo1-Cl3-Ag1, 151.39(10); Mo1-Cl4-Ag1, 158.06(9) Averaged = 154.725
$(1,4\text{-}BDA)_2AgRuCl_8$ (**5**)	
bond lengths **axial bonds:** Ru1-Cl1 = 2.360(3) Ag1-Cl2 = 2.509(4) **equatorial bonds:** Ru1-Cl3 = 2.355(3) Ru1-Cl4 = 2.377(4) Ag1-Cl3 = 2.852(3) Ag1-Cl4 = 2.906(4)	**bond angles** **axial *cis* bonds:** Cl1-Ru1-Cl3 = 90.0; Cl1-Ru1-Cl4 = 89.80(11) & 90.20(11) Cl2-Ag1-Cl3 = 90.0; Cl2-Ag1-Cl4 = 89.31(12) & 90.69(12) **equatorial *cis* bonds:** Cl3-Ru1-Cl4 = 90 Cl3-Ag1-Cl4 = 90 ***trans* bonds (axial & equatorial):** Cl1-Ru1-Cl1 = Cl3-Ru1-Cl3 = Cl4-Ru1-Cl4 = Cl2-Ag1-Cl2 = Cl3-Ag1-Cl3 = Cl4-Ag1-Cl4 = 180.0 **in-plane bridging bonds:** Ru1-Cl4-Ag1 = 164.17(14), Ru1-Cl3-Ag1 = 180.00 Averaged = 172.085
$(1,4\text{-}BDA)_2AgRuBr_8$ (**6**)	
bond lengths **axial bonds:** Ru1-Br1 = 2.508(3) Ag1-Br2 = 2.544(3) **equatorial bonds:** Ru1-Br3 = 2.532(3) Ru1-Br4 = 2.531(2) Ag1-Br3 = 3.123(4) Ag1-Br4 = 3.126(4)	**bond angles** **axial *cis* bonds:** Br1-Ru1-Br3 = 89.90(8) & 90.10(8); Br1-Ru1-Br4 = 88.94(8) & 91.06(8) Br2-Ag1-Br3 = 88.00(7) & 92.00(7); Br2-Ag1-Br4 = 89.55(7) & 90.45(7) **equatorial *cis* bonds:** Br3-Ru1-Br4 = 89.94(11) & 90.06(11) Br3-Ag1-Br4 = 88.84(10) & 91.16(10) ***trans* bonds (axial & equatorial):** Br1-Ru1-Br1 = Br3-Ru1-Br3 = Br4-Ru1-Br4 = Br2-Ag1-Br2 = Br3-Ag1-Br3 = Br4-Ag1-Br4 = 180 **in-plane bridging bonds:** Ru1-Br3-Ag1 = 165.83(8), Ru1-Br4-Ag1 = 166.18(8) Averaged = 166.00
$(1,3\text{-}PDA)_2AgRuCl_8$ (**7**) 300 K	

bond lengths **axial bonds:** Ru1-Cl1 = 2.362(2) Ag1-Cl2 = 2.518(3) **equatorial bonds:** Ru1-Cl3 = 2.360(2) Ru1-Cl4 = 2.367(2) Ag1-Cl3 = 2.856(2) Ag1-Cl4 = 2.930(2)	**bond angles** **axial *cis* bonds:** Cl1-Ru1-Cl3 = 90.0; Cl1-Ru1-Cl4 = 89.67(11) & 90.33(11) Cl2-Ag1-Cl3 = 90.0; Cl2-Ag1-Cl4 = 88.88(11) & 91.12(11) **equatorial *cis* bonds:** Cl3-Ru1-Cl4 = 90.0 Cl3-Ag1-Cl4 = 90.0 ***trans* bonds (axial & equatorial):** Cl1-Ru1-Cl1 = Cl3-Ru1-Cl3 = Cl4-Ru1-Cl4 = Cl2-Ag1-Cl2 = Cl3-Ag1-Cl3 = Cl4-Ag1-Cl4 = 180.0 **in-plane bridging bonds:** Ru1-Cl4-Ag1 = 164.04(13), Ru1-Cl3-Ag1 = 180.00 Averaged = 172.05
$(1,3\text{-PDA})_2AgRuCl_8$ (**7**) 220 K	
bond lengths **axial bonds:** Ru1-Cl1 = 2.371(3) Ag1-Cl3 = 2.454(3) **equatorial bonds:** Ru1-Cl2 = 2.378(2) Ag1-Cl2 = 3.0050(19)	**bond angles** **axial *cis* bonds:** Cl1-Ru1-Cl2 = 89.58(6) & 90.42(6) Cl2-Ag1-Cl3 = 88.28(7) & 91.72(7) **equatorial *cis* bonds:** Cl2-Ru1-Cl2 = 88.66(10) & 91.34(10) Cl2-Ag1-Cl2 = 99.99(8) & 80.01(8) ***trans* bonds (axial & equatorial):** Cl1-Ru1-Cl1 = Cl2-Ru1-Cl2 = Cl2-Ag1-Cl2 = Cl3-Ag1-Cl3 = 180.0 **in-plane bridging bonds:** Ru1-Cl3-Ag1 = 162.35(7) Average = 162.35(7)
$(1,3\text{-PDA})_2AgRuBr_8$ (8)	
bond lengths **axial bonds:** Ru1-Br1 = 2.5178(14) Ag1-Br2 = 2.5576(16) **equatorial bonds:** Ru1-Br3 = 2.5139(10) Ag1-Br3 = 3.0991(13)	**bond angles** **axial *cis* bonds:** Br1-Ru1-Br3 = 89.84(4) & 90.16(4) Br2-Ag1-Br3 = 88.11(4) & 91.89 (4) **equatorial *cis* bonds:** Br3-Ru1-Br3, 88.74(6) & 91.26(6) Br3-Ag1-Br3, 80.46(5) & 99.54(5) ***trans* bonds (axial & equatorial):** Br1-Ru1-Br1 = Br3-Ru1-Br3 = Br2-Ag1-Br2 = Br3-Ag1-Br3 = 180.0 **in-plane bridging bonds:** Ru1-Br3-Ag1 = 162.84(5) Average = 162.84(5)

Table S4. Shortest distances between halogen and nitrogen, N···*X* distances (Å) in the layered halides **1**-**8**.

$(PPDA)_2AgRuCl_8$ (**1**)
With axial chlorides: 3.136(5), 3.280(5), 3.907(5), 4.452(6) **With equatorial chlorides:** 3.275(5), 3.329(5), 3.556(5), 3.776(5)
$(PPDA)_2CuRuCl_8$ (**2**)
With axial chlorides: 3.290(11), 3.293(12), 3.416(11), 3.590(11) **With equatorial chlorides:** 3.184(9), 3.320(13), 3.847(13), 4.489(9)
$(PPDA)_2AgRuBr_8$ (**3**)
With axial bromides: 3.32(3), 3.40(3), 4.22(3), 4.59(3) **With equatorial bromides:** 3.46(3), 3.52(3), 3.53(3), 4.33(3)
$(PPDA)_2AgMoCl_8$ (**4**)
With axial chlorides: 3.055(15), 3.25(3), 4.06(3), 4.562(15), **With equatorial chlorides:** 3.285(18), 3.299(18), 3.742(18), 3.935(19)
$(1,4\text{-}BDA)_2AgRuCl_8$ (**5**)
With axial chlorides: 3.253(10), 3.361(10), 4.031(10), 4.169(10) **With equatorial chlorides:** 3.337(10), 3.338(9), 3.470(9), 3.449(9)
$(1,4\text{-}BDA)_2AgRuBr_8$ (**6**)
With axial bromides: 4.093(15), 3.318(13), 3.870(15), 4.637(13) **With equatorial bromides:** 3.562(13), 3.589(15), 3.606(15), 3.762(13)
$(1,3\text{-}PDA)_2AgRuCl_8$ (**7**) 300K
With axial chlorides: 3.206(8), 3.346(8), 4.064(8), 4.233(8) **With equatorial chlorides:** 3.338(6), 3.444(7), 3.460(9), 3.376(7)
$(1,3\text{-}PDA)_2AgRuCl_8$ (**7**) 220K
This compound has two crystallographic unique NH_3^+ groups - the distances of each nitrogen to the Cl ligands are given separately **N(1)···Cl** **With axial chlorides:** 3.211(10), 3.5995(8), 4.653(10) **With equatorial chlorides:** 3.360(17), 3.612(13) **N(2)···Cl** **With axial chlorides:** 3.205(10), 3.6179(12) **With equatorial chlorides:** 3.628(7), 3.323(5)
$(1,3\text{-}PDA)_2AgRuBr_8$ (**8**)
This compound has two crystallographic unique NH_3^+ groups - the distances of each nitrogen to the Br ligands are given separately **N(1)···Br** **With axial bromides:** 3.372(15), 3.7669(17), 4.811(15) **With equatorial bromides:** 3.493(10), 3.617(12) **N(2)···Br** **With axial bromides:** 3.348(14), 3.784(3), 4.846(13) **With equatorial bromides:** 3.521(12), 3.757(9)

Bond distortion levels (Δ*d*): It was calculated from the following equation. [S13]

$$\Delta\, d = \frac{1}{6} \sum[(d_i - d)/d]^2$$

where, d_i is the length of i^{th} *M-X* bond, *d* is the averaged *M-X* bond length.

The bond angle variance (σ^2) was calculated from following reaction. [S14]

$$\sigma^2 = \sum_{i=1}^{12} (\theta_i - 90)^2/11$$

θ_i is the i^{th} *X-M-X* bond angle.

The values are given in the table S5 below.

Table S5. Bond distortion levels and bond angle variance for **1-8**. Both bond distortion level and bond angle variance are higher for the M^I metal, indicating higher distortions around it.

compounds	**Bond distortion level (Δ*d*)**	**Bond angle variance (σ^2)**
$(PPDA)_2AgRuCl_8$ (**1**)	$[RuCl_6] = 5.52 \times 10^{-6}$ $[AgCl_6] = 7.35 \times 10^{-3}$	$[RuCl_6] = 1.018$ $[AgCl_6] = 30.027$
$(PPDA)_2CuRuCl_8$ (**2**)	$[RuCl_6] = 3.67 \times 10^{-6}$ $[CuCl_6] = 18.01 \times 10^{-3}$	$[RuCl_6] = 1.030$ $[CuCl_6] = 33.612$
$(PPDA)_2AgRuBr_8$ (**3**)	$[RuBr_6] = 3.96 \times 10^{-6}$ $[AgBr_6] = 6.89 \times 10^{-3}$	$[RuBr_6] = 0.714$ $[AgBr_6] = 32.975$
$(PPDA)_2AgMoCl_8$ (**4**)	$[MoCl_6] = 4.37 \times 10^{-6}$ $[AgCl_6] = 7.52 \times 10^{-3}$	$[MoCl_6] = 0.742$ $[AgCl_6] = 28.631$
$(1,4\text{-}BDA)_2AgRuCl_8$ (**5**)	$[RuCl_6] = 15.43 \times 10^{-6}$ $[AgCl_6] = 4.11 \times 10^{-3}$	$[RuCl_6] = 0.014$ $[AgCl_6] = 0.173$
$(1,4\text{-}BDA)_2AgRuBr_8$ (**6**)	$[RuBr_6] = 20.97 \times 10^{-6}$ $[AgBr_6] = 8.74 \times 10^{-3}$	$[RuBr_6] = 0.413$ $[AgBr_6] = 2.017$
$(1,3\text{-}PDA)_2AgRuCl_8$ (**7**) 300 K	$[RuCl_6] = 1.55 \times 10^{-6}$ $[AgCl_6] = 4.19 \times 10^{-3}$	$[RuCl_6] = 0.039$ $[AgCl_6] = 0.456$
$(1,3\text{-}PDA)_2AgRuCl_8$ (**7**) 200 K	$[RuCl_6] = 20.97 \times 10^{-6}$ $[AgCl_6] = 8.72 \times 10^{-3}$	$[RuCl_6] = 0.673$ $[AgCl_6] = 39.646$
$(1,3\text{-}PDA)_2AgRuBr_8$ (**8**)	$[RuBr_6] = 0.56 \times 10^{-6}$ $[AgBr_6] = 7.63 \times 10^{-3}$	$[RuBr_6] = 0.595$ $[AgBr_6] = 35.693$

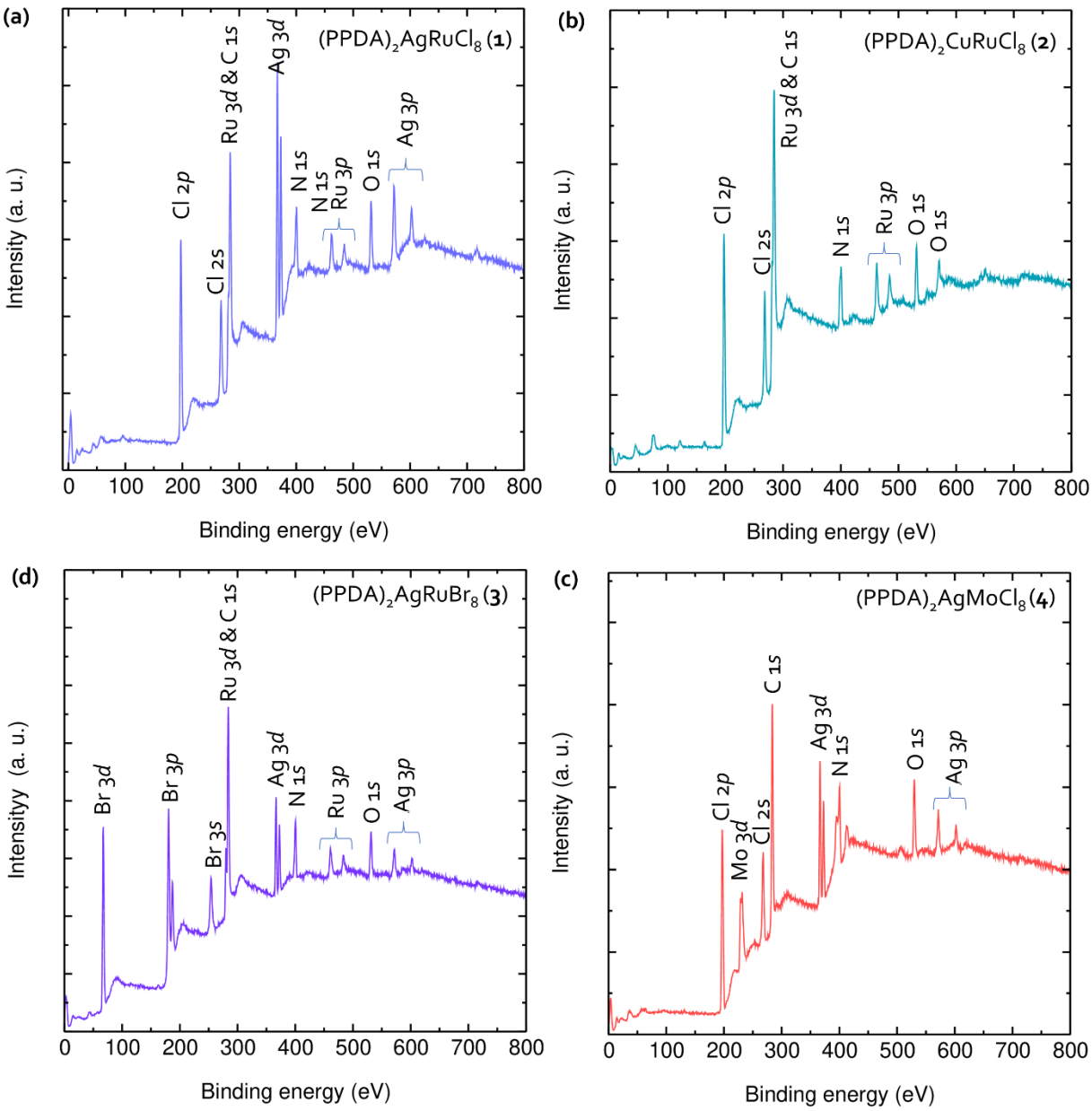

Figure S1. XPS survey spectra of **1**-**4**.

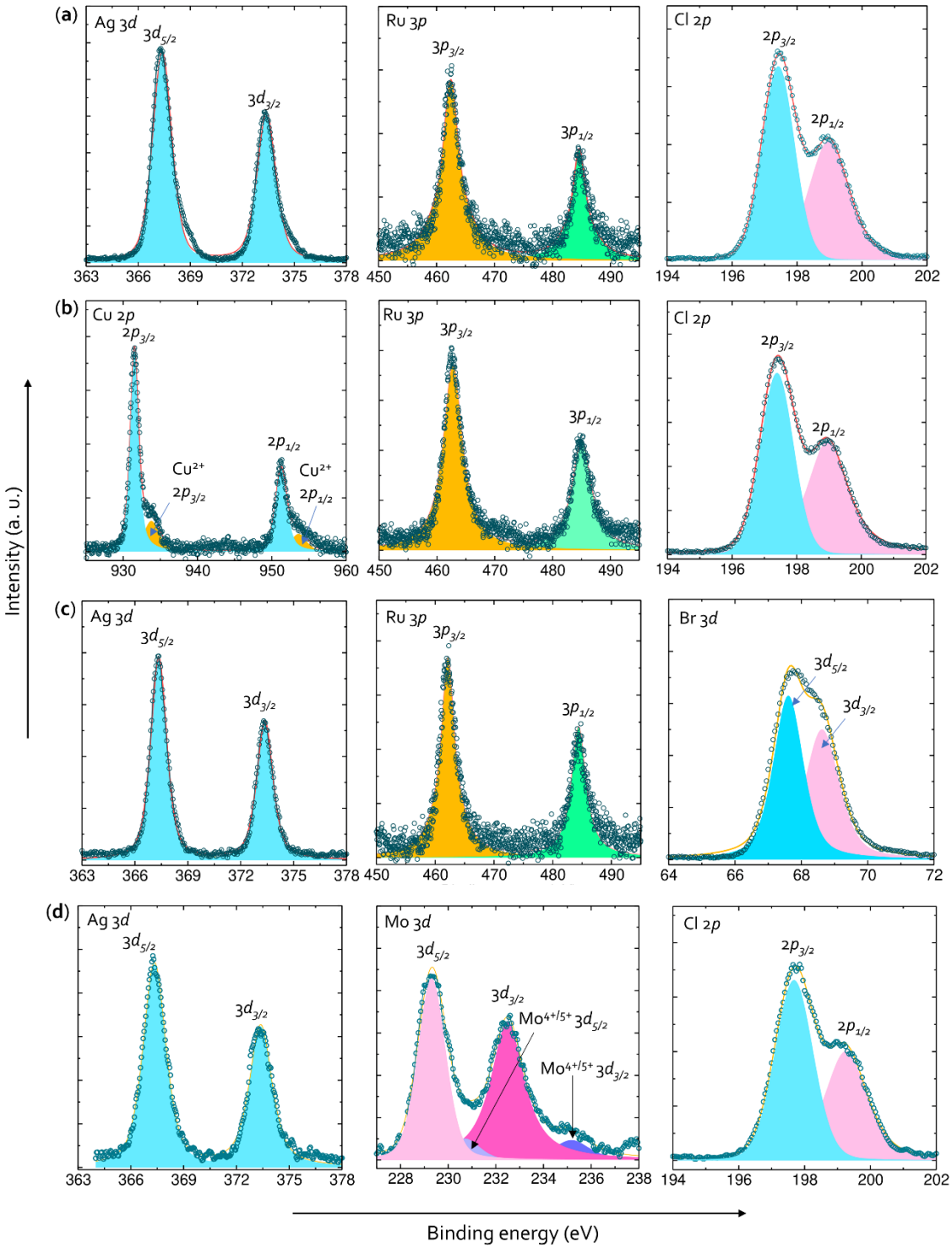

Figure S2. Core level XPS of (a) $(PPDA)_2AgRuCl_8$ (**1**), (b) $(PPDA)_2CuRuCl_8$ (**2**), (c) $(PPDA)_2AgRuBr_8$ (**3**) and (d) $(PPDA)_2AgMoCl_8$ (**4**). Three panels in each compound show the core level spectra of M^{I} metal, M^{III} metal and X halide.

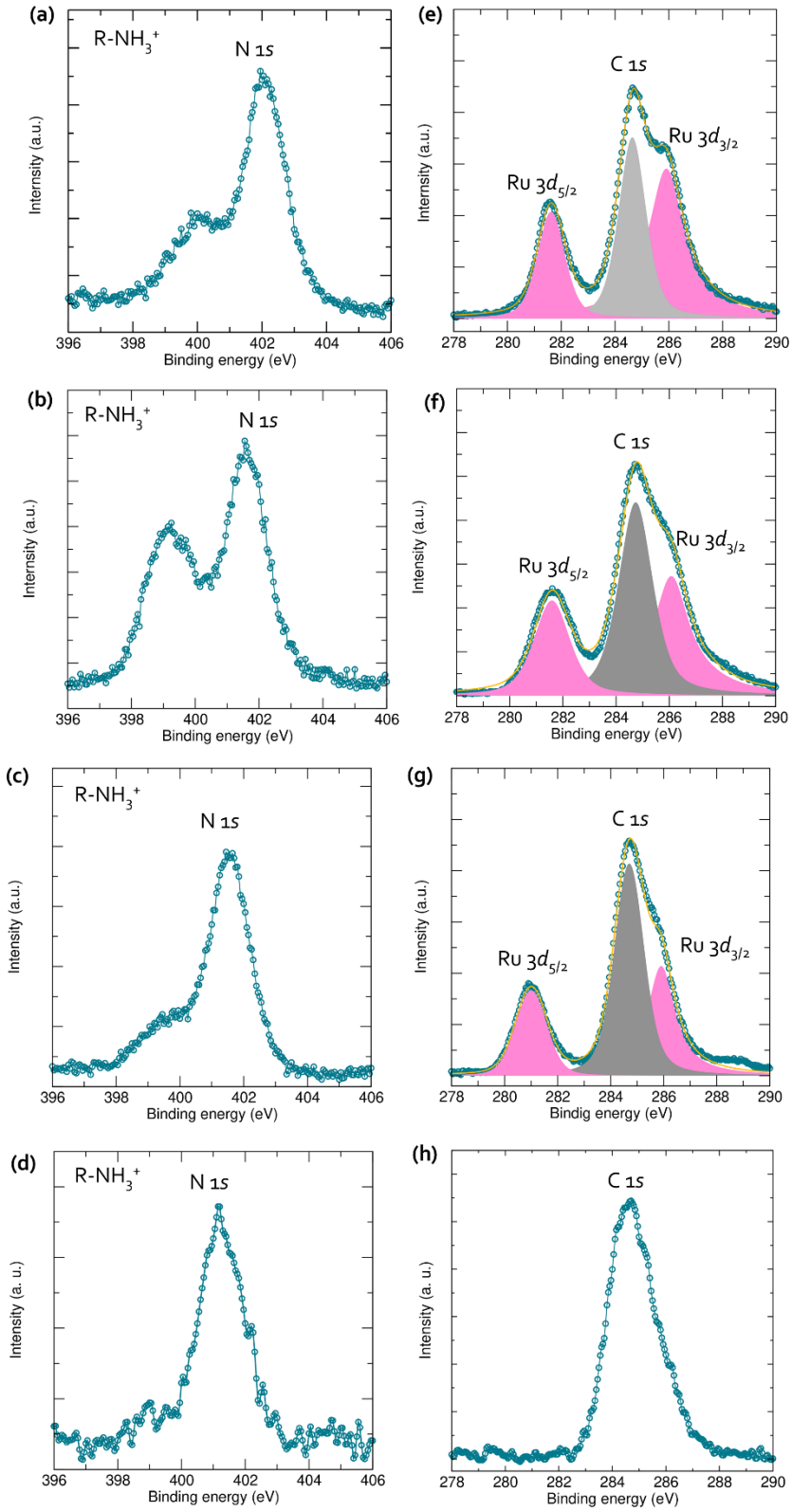

Figure S3. Core level N 1*s* XPS of (a) $(PPDA)_2AgRuCl_8$ (**1**), (b) $(PPDA)_2CuRuCl_8$ (**2**), (c) $(PPDA)_2AgRuBr_8$ (**3**) and (d) $(PPDA)_2AgMoCl_8$ (**4**). Core level Ru $3d_{5/2}$, Ru $3d_{5/2}$ and C 1*s* XPS of (e) $(PPDA)_2AgRuCl_8$ (**1**), (f) $(PPDA)_2CuRuCl_8$ (**2**), (g) $(PPDA)_2AgRuBr_8$ (**3**) and (d) $(PPDA)_2AgMoCl_8$ (**4**).

Table S6. Binding energies (eV) obtained from XPS data.

XPS peaks	$(PPDA)_2AgRuCl_8$ (**1**)	$(PPDA)_2CuRuCl_8$ (**2**)	$(PPDA)_2AgRuBr_8$ (**3**)	$(PPDA)_2AgMoCl_8$ (**4**)
Ag $3d_{5/2}$	367.3	-	367.3	367.3
Ag $3d_{3/2}$	373.3	-	373.3	373.4
Cu $2p_{3/2}$	-	932.1	-	-
Cu $2p_{1/2}$	-	951.0	-	-
Ru $3p_{3/2}$	462.7	462.4	462.1	-
Ru $3p_{1/2}$	485.2	484.6	484.5	-
Mo $3d_{5/2}$	-	-	-	229.3
Mo $3d_{3/2}$	-	-	-	232.5
Cl $2p_{3/2}$	197.9	197.4	-	197.7
Cl $2p_{1/2}$	199.4	198.9	-	199.3
Br $3d_{5/2}$	-	-	67.9	-
Br $3d_{3/2}$	-	-	68.9	-
Ru $3d_{5/2}$	281.6	281.6	280.9	-
Ru $3d_{3/2}$	285.9	285.8	285.7	-
C $1s$	284.6	284.6	284.6	284.6
N $1s$	401.6	401.6	401.6	401.2

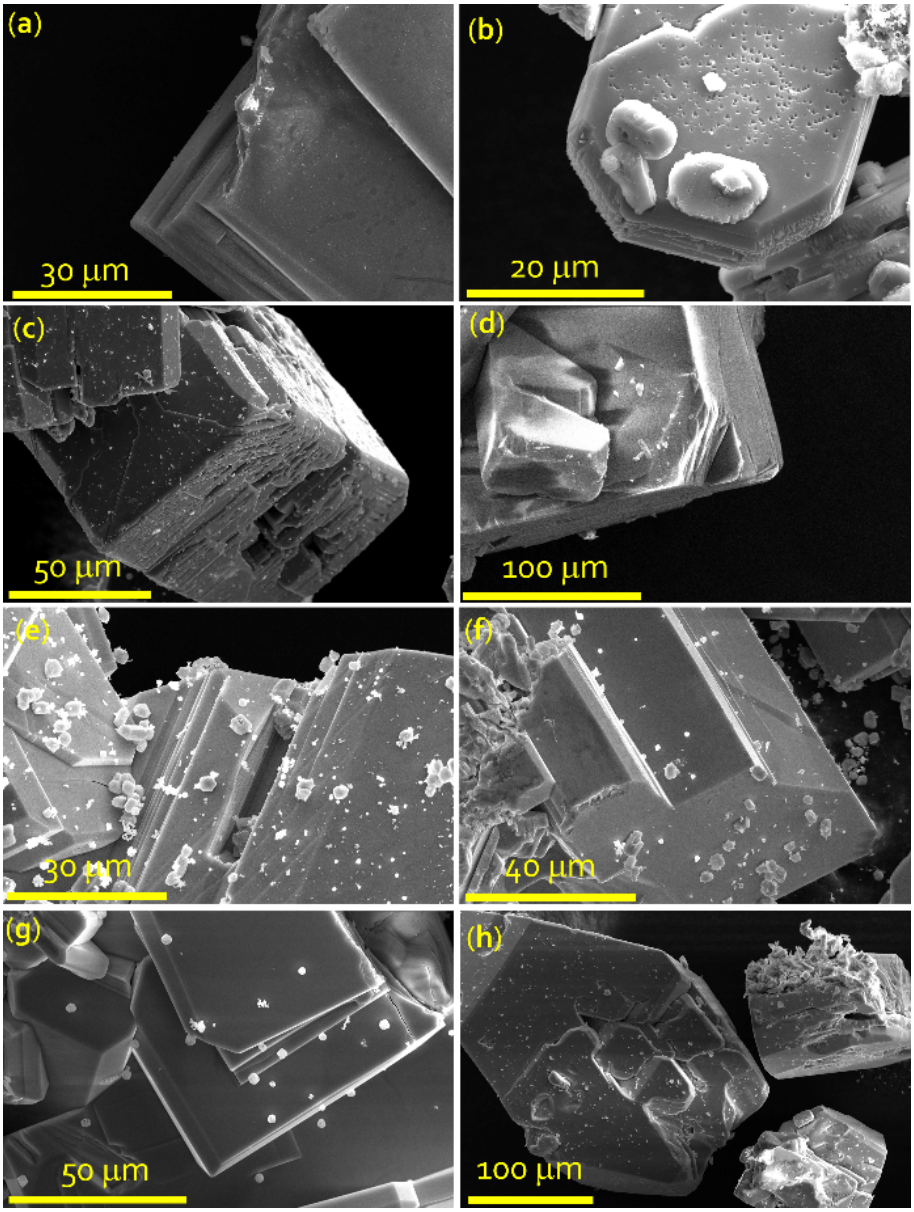

Figure S4. SEM images of (a) $(PPDA)_2AgRuCl_8$ (**1**), (b) $(PPDA)_2CuRuCl_8$ (**2**), (c) $(PPDA)_2AgRuBr_8$ (**3**), (d) $(PPDA)_2AgMoCl_8$ (**4**), (e) $(1,4\text{-}BDA)_2AgRuCl_8$ (**5**), (f) $(1,4\text{-}BDA)_2AgRuBr_8$ (**6**), (g) $(1,3\text{-}PDA)_2AgRuCl_8$ (**7**), and (h) $(1,3\text{-}PDA)_2AgRuBr_8$ (**8**). These images show layered morphology of perovskites.

Layer twisting: We found that the compounds **1**-**4** show difference in M^{I}-X-M^{III} bond angles and octahedral tilting which deviate more from 180° with larger metal or smaller halide. We show that these deviations increase as the average radius ratio $[(0.5rM^{I} + 0.5rM^{III})/rX]$ increases, while the out-of-plane tilting changes only marginally.

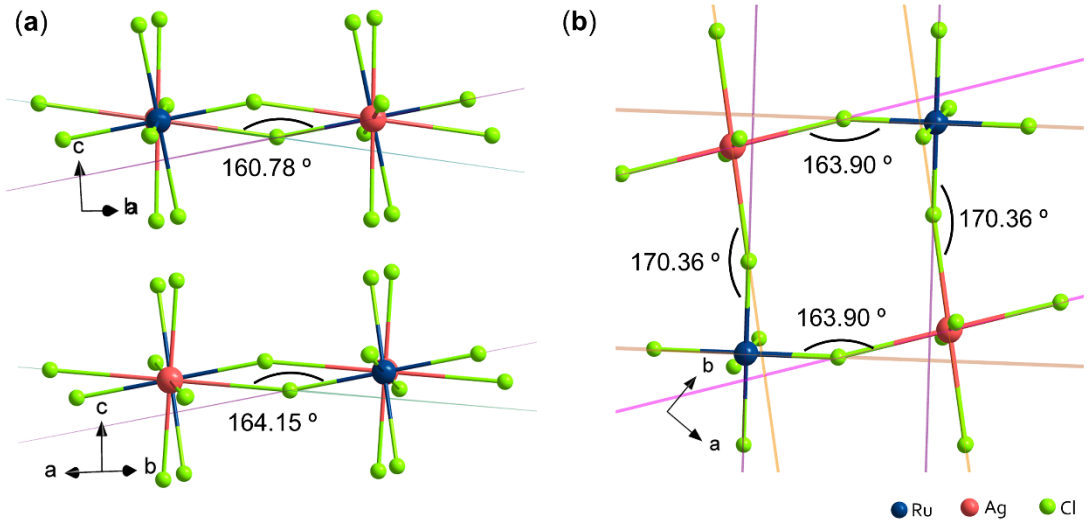

Figure S5. Octahedral tilting in $(PPDA)_2AgRuCl_8$ (**1**). (**a**) out-of-plane tilting wherein the angle 160.78 ° is between the planes passing through Ru1, Ag1 and Cl3 atoms, and the angle 164.15 ° is between the planes passing through Ru1, Ag1 and Cl4 atoms. (**b**) in-plane tilting wherein the angle 163.90 ° is between the planes passing through Ag1 and Cl3 atoms of two neighbouring perovskite layers, and Ru1 and Cl3 atoms of two neighbouring perovskite layers, and the angle 170.36 ° is between the planes passing through Ag1 and Cl4 atoms of two neighbouring perovskite layers, and Ru1 and Cl4 atoms of two neighbouring perovskite layers.

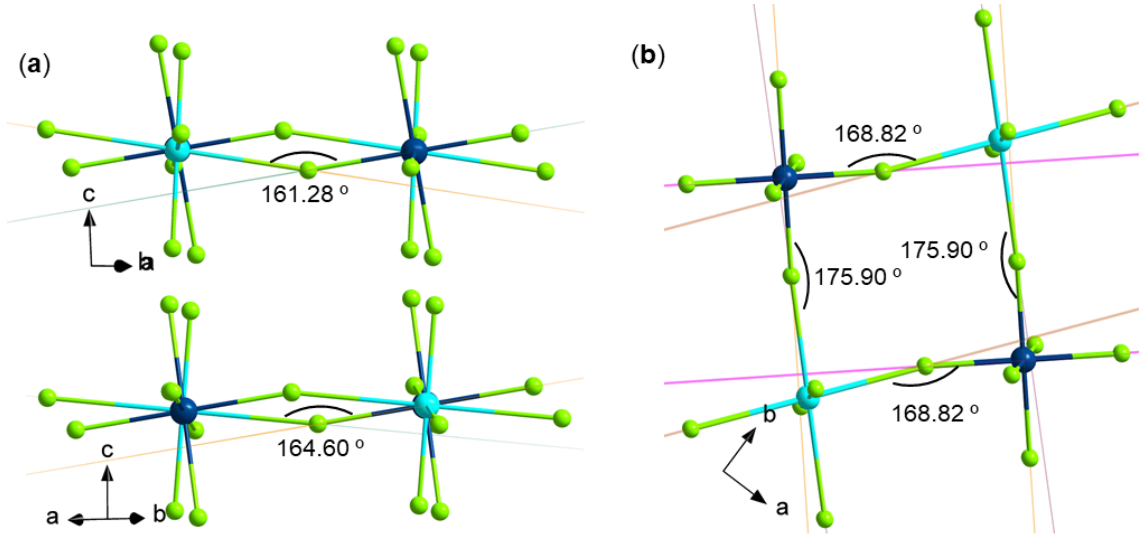

Figure S6. Octahedral tilting in $(PPDA)_2CuRuCl_8$ (**2**). (**a**) out-of-plane tilting wherein the angle 161.28 ° is between the planes passing through Ru1, Cu1 and Cl4 atoms, and the angle 164.60 ° is between the planes passing through Ru1, Cu1 and Cl3 atoms. (**b**) in-plane tilting wherein the angle 168.82 ° is between the planes passing through Cu1, Cl3 atoms of two neighbouring perovskite layers, and Ru1, Cl3 atoms of two neighbouring perovskite layers, and the angle 175.90 ° is between the planes passing through Cu1, Cl4 atoms of two neighbouring perovskite layers, and Ru1, Cl4 atoms of two neighbouring perovskite layers.

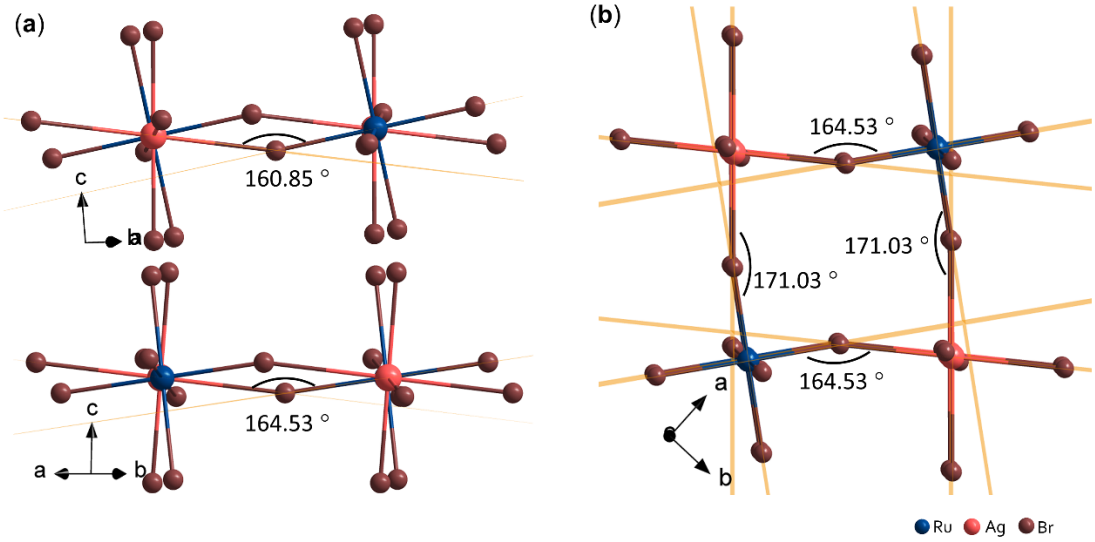

Figure S7. Octahedral tilting in $(PPDA)_2AgRuBr_8$ (**3**). (**a**) out-of-plane tilting wherein the angle 160.85 ° is between the planes passing through Ru1, Cu1 and Cl3 atoms, and the angle 164.53 ° is between the planes passing through Ru1, Ag1 and Br4 atoms. (**b**) in-plane tilting wherein the angle 171.03 ° is between the planes passing through Ag1, Br3 atoms of two neighbouring perovskite layers, and Ru1, Br3 atoms of two neighbouring perovskite layers, and the angle 164.53° is between the planes passing through Ag1, Br4 atoms of two neighbouring perovskite layers, and Ru1, Br4 atoms of two neighbouring perovskite layers.

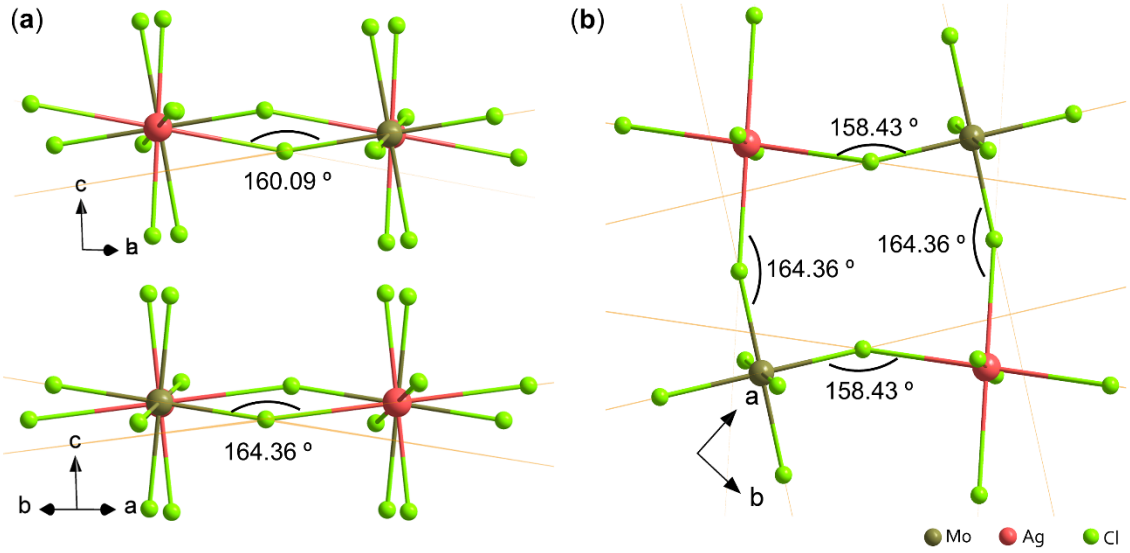

Figure S8. Octahedral tilting in $(PPDA)_2AgMoCl_8$ (**4**). (**a**) out-of-plane tilting wherein the angle 160.09 ° is between the planes passing through Ru1, Cu1 and Cl3 atoms, and the angle 164.36 ° is between the planes passing through Mo1, Ag1 and Cl4 atoms. (**b**) in-plane tilting wherein the angle 158.43 ° is between the planes passing through Ag1, Cl3 atoms of two neighbouring perovskite layers, and Mo1, Cl3 atoms of two neighbouring perovskite layers, and the angle 164.36° is between the planes passing through Ag1, Cl4 atoms of two neighbouring perovskite layers, and Mo1, Cl4 atoms of two neighbouring perovskite layers.

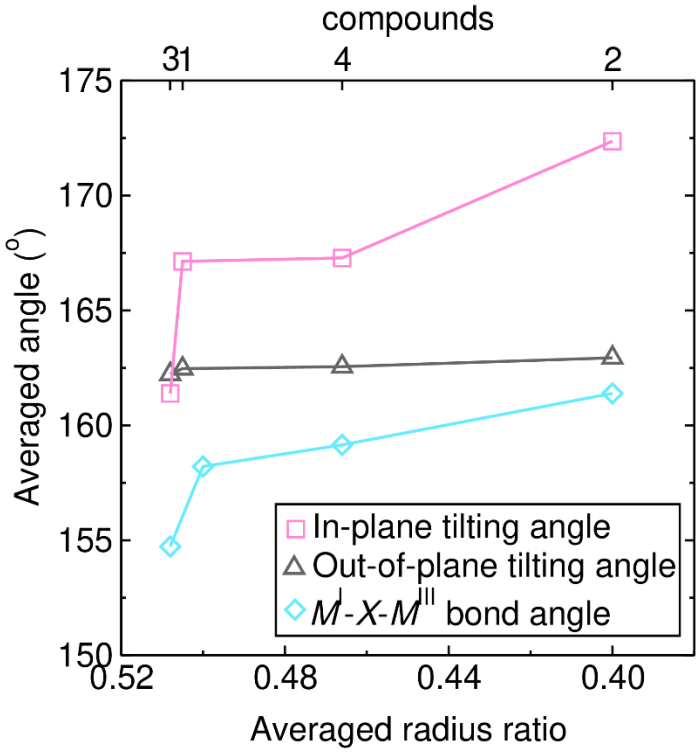

Figure S9. Plots showing averaged in-plane tilting, averaged out-of-plane tilting and averaged M^{I}-X-M^{III} bond angles versus the averaged radius ratio in **1**-**4**. The averaged radius ratio is calculated using the formula $[(0.5rM^{I} + 0.5rM^{III})]/rX$, where rM^{I}, rM^{III}, rX denote the radii of the monovalent metal, trivalent metal and the halide, respectively.

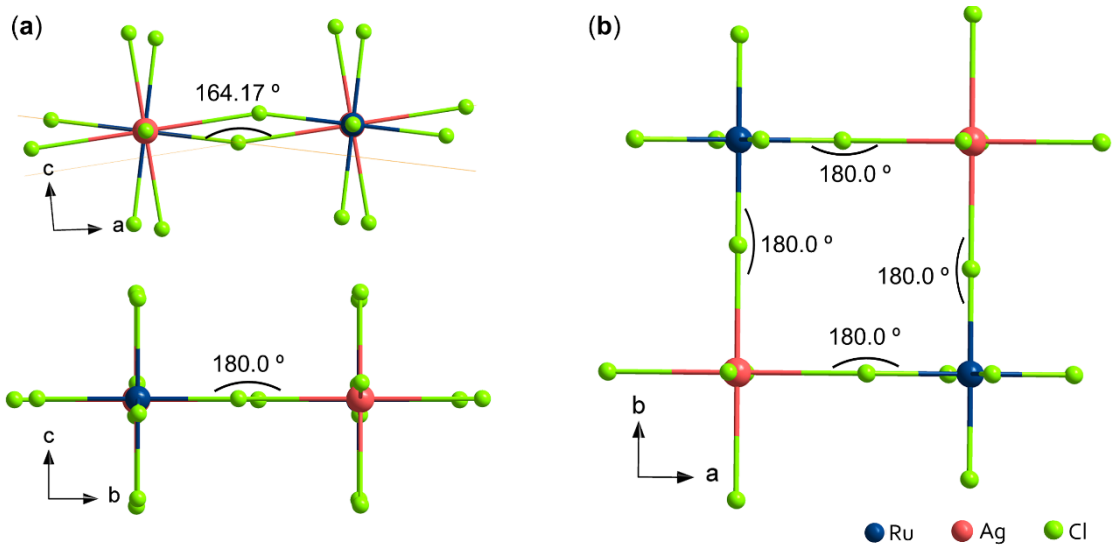

Figure S10. Octahedral tilting in $(1,4\text{-BDA})_2AgRuCl_8$ (**5**). (**a**) out-of-plane tilting wherein the angle 164.17 ° is between the planes passing through Ru1, Ag1 and Cl4 atoms, and the angle 180.0 ° is between the planes passing through Ru1, Ag1 and Cl3 atoms. (**b**) in-plane tilting wherein the angle 180.0 ° is between the planes passing through Ru1, Ag1, Cl3 atoms of two neighbouring perovskite layers, and Ru1, Ag1, Cl4 atoms of two neighbouring perovskite layers, and the angle 180.0° is between the planes passing through Ru1, Ag1, Cl4 atoms of two neighbouring perovskite layers, and Ru1, Ag1, Cl4 atoms of two neighbouring perovskite layers.

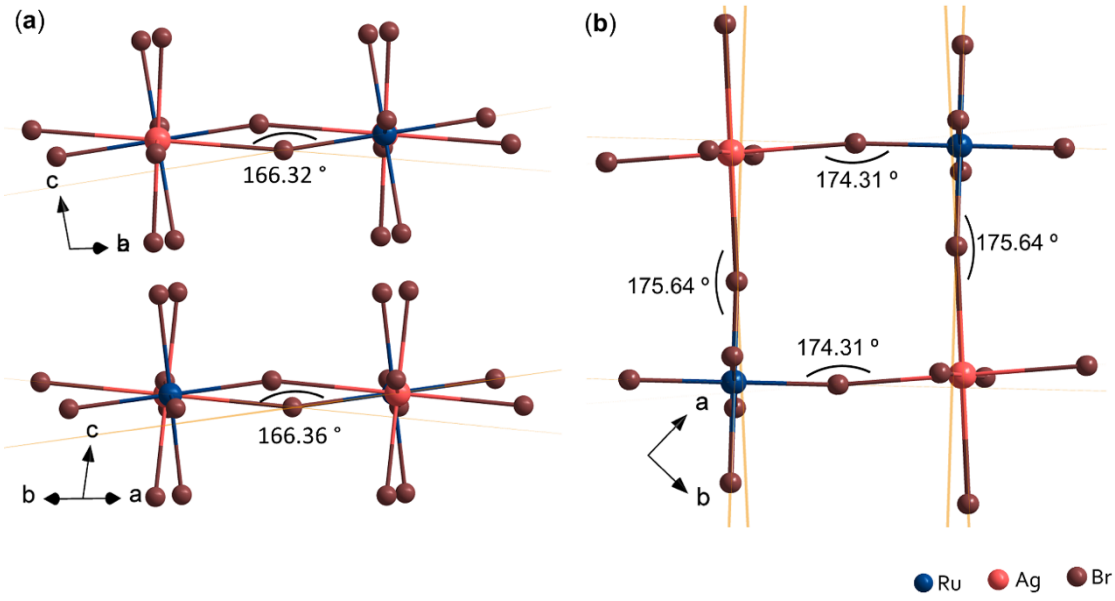

Figure S11. Octahedral tilting in $(1,4\text{-BDA})_2AgRuBr_8$ (**6**). (**a**) out-of-plane tilting wherein the angle 166.32 ° is between the planes passing through Ru1, Ag1 and Br3 atoms, and the angle 166.36 ° is between the planes passing through Ru1, Ag1 and Br4 atoms. (**b**) in-plane tilting wherein the angle 175.64 ° is between the planes passing through Ru1, Ag1, Br4 atoms of two neighbouring perovskite layers, and Ru1, Ag1, Br4 atoms of two neighbouring perovskite layers, and the angle 174.31° is between the planes passing through Ru1, Ag1, Br3 atoms of two neighbouring perovskite layers, and Ru1, Ag1, Br3 atoms of two neighbouring perovskite layers.

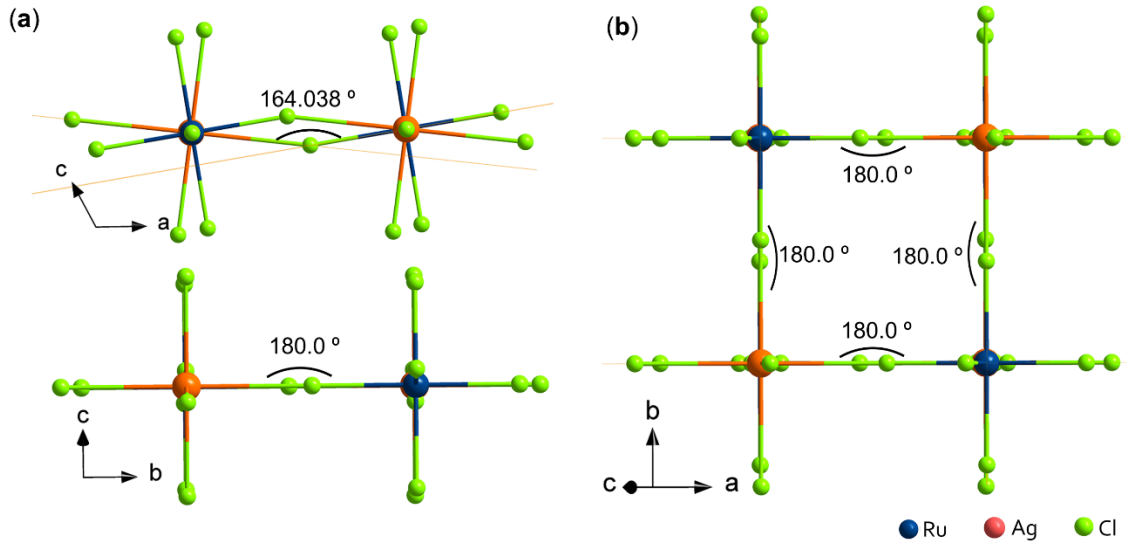

Figure S12. Octahedral tilting in (1,3-PDA)$_2$AgRuCl$_8$ (**7**). (**a**) out-of-plane tilting wherein the angle 164.038 ° is between the planes passing through Ru1, Ag1 and Cl4 atoms, and the angle 180.0 ° is between the planes passing through Ru1, Ag1 and Cl3 atoms. (**b**) in-plane tilting wherein the angle 180.0 ° is between the planes passing through Ru1, Ag1, Cl3 atoms of two neighbouring perovskite layers, and Ru1, Ag1, Cl4 atoms of two neighbouring perovskite layers, and the angle 180.0° is between the planes passing through Ru1, Ag1, Cl4 atoms of two neighbouring perovskite layers, and Ru1, Ag1, Cl4 atoms of two neighbouring perovskite layers.

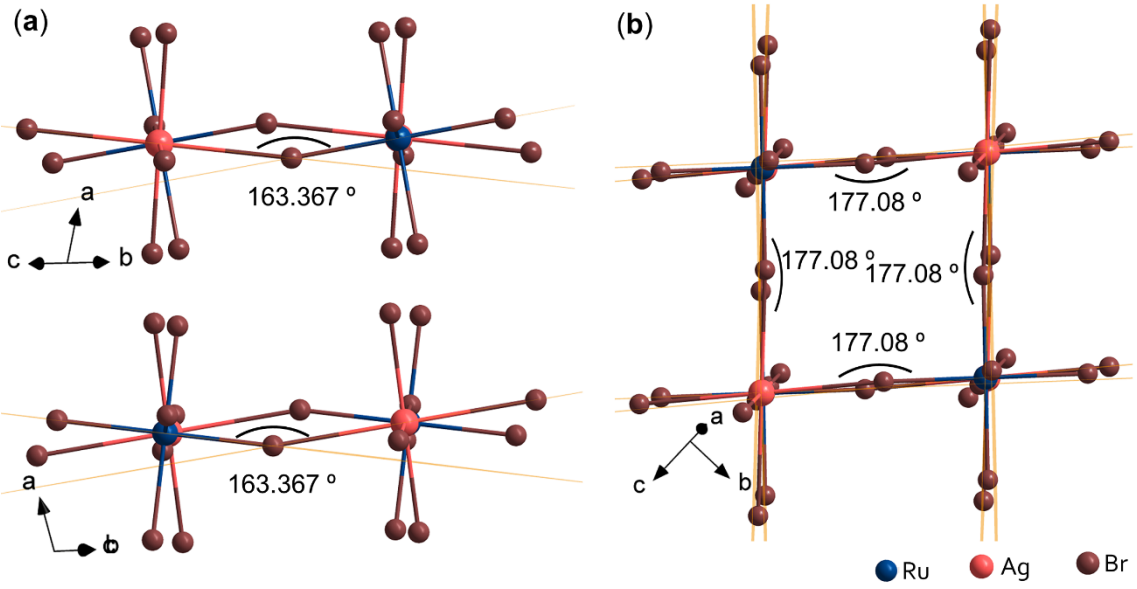

Figure S13. Octahedral tilting in (1,3-PDA)$_2$AgRuBr$_8$ (**8**). (**a**) out-of-plane tilting wherein the angle 163.367 ° is between the planes passing through Ru1, Ag1 and Br3 atoms, and the angle 163.367 ° is between the planes passing through Ru1, Ag1 and Br3 atoms. (**b**) in-plane tilting wherein the angle 177.08 ° is between the planes passing through Ru1, Ag1, Br3 atoms of two neighbouring perovskite layers, and Ru1, Ag1, Br3 atoms of two neighbouring perovskite layers, and the angle 177.08° is between the planes passing through Ru1, Ag1, Br3 atoms of two neighbouring perovskite layers, and Ru1, Ag1, Br3 atoms of two neighbouring perovskite layers.

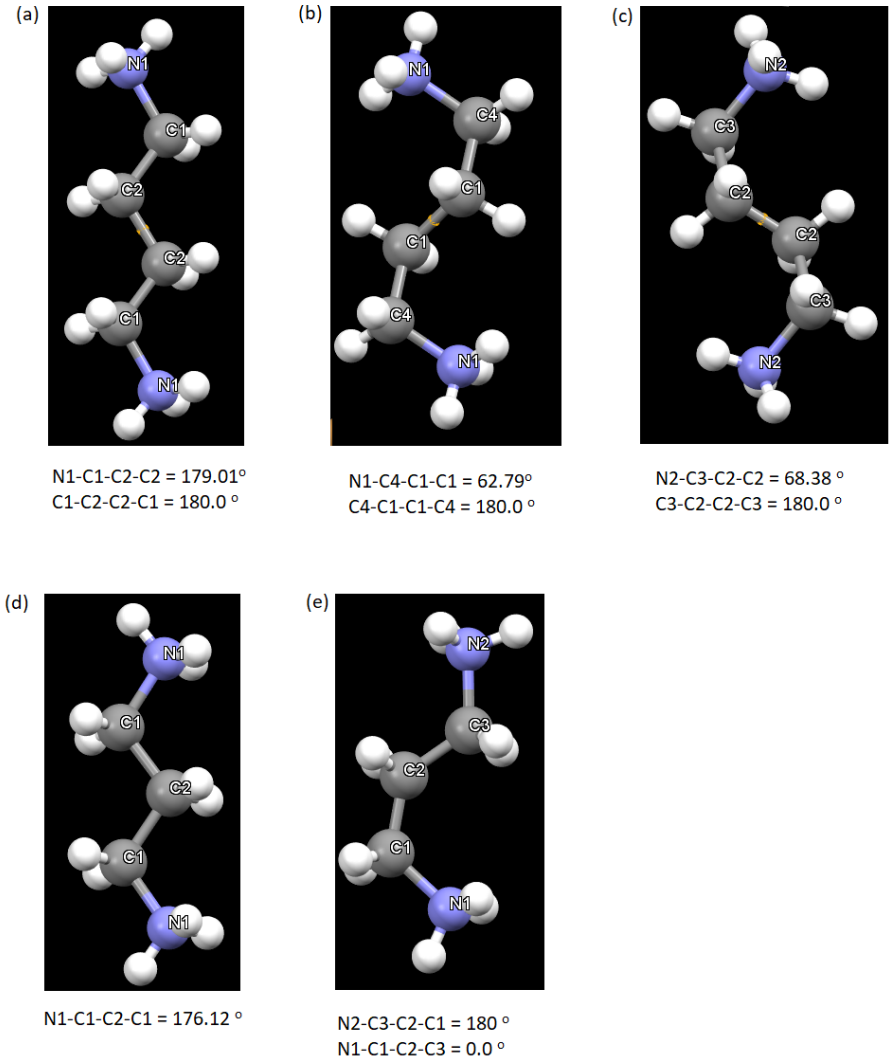

Figure S14. Conformations of 1,4-BDA and 1,3-PDA in the perovskites, **5-8.** (a) *anti* conformation of 1,4-BDA in **5,** (b, c) crystallographically two different 1,4-BDA cations in **6**, (d) *anti* conformation of 1,3-PDA in **7,** (e) on one end *anti* and other end *eclipsed* conformation of 1,3-PDA in **7** at 220 K as well as in **8** at room temperature. Torsion angles are also given.

Phase transition in (1,3-PDA)$_2$AgRuCl$_8$ (7). We examined the compound **7** if the conformational changes can occur within the same compound with the help of external stimuli such as change in the temperature. Prior to x-ray diffraction, we performed thermogravimetric analysis (TGA) and differential scanning calorimetry (DSC). The TGA suggested that the material is stable upto ~ 525 K. Before the decomposition temperature, the DSC profile shows an exothermic peak at ~ 235 K

on cooling and an endothermic peak at ~ 300 K on heating, pointing towards a possible phase transition. We cooled the crystal below 235 K and measured the low temperature (220 K) structure. The space group and the layer stacking pattern remain unchanged on cooling, but the spacer changes its conformation to bent (**Figure S15**) one which is like the one found in bromide analogue **8**.

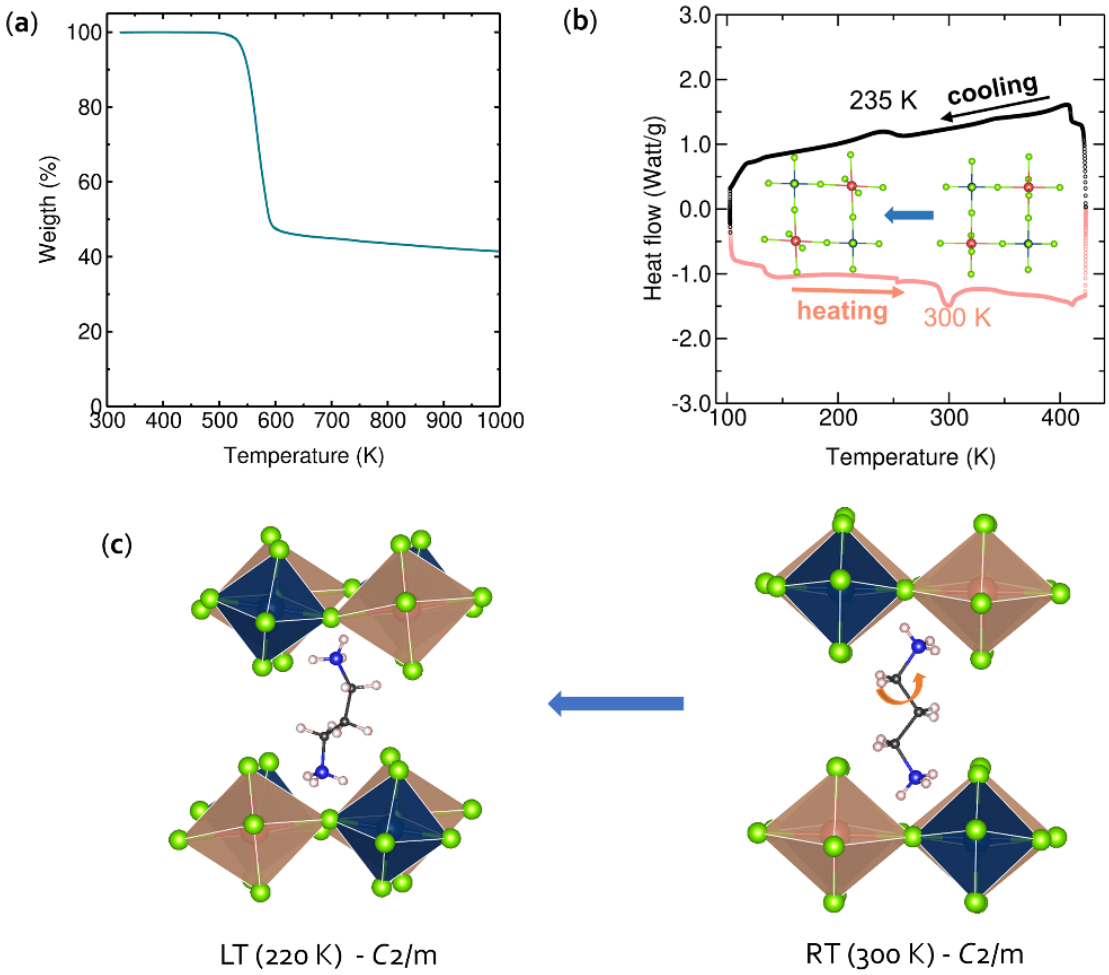

Figure S15. (a) TGA plot of $(1,3\text{-PDA})_2AgRuCl_8$ (**7**). (b) DSC plot of **7** showing an exothermic peak at 235 K on cooling and endothermic peak at 300 K on heating. (c) Showing two different phases of **7**.

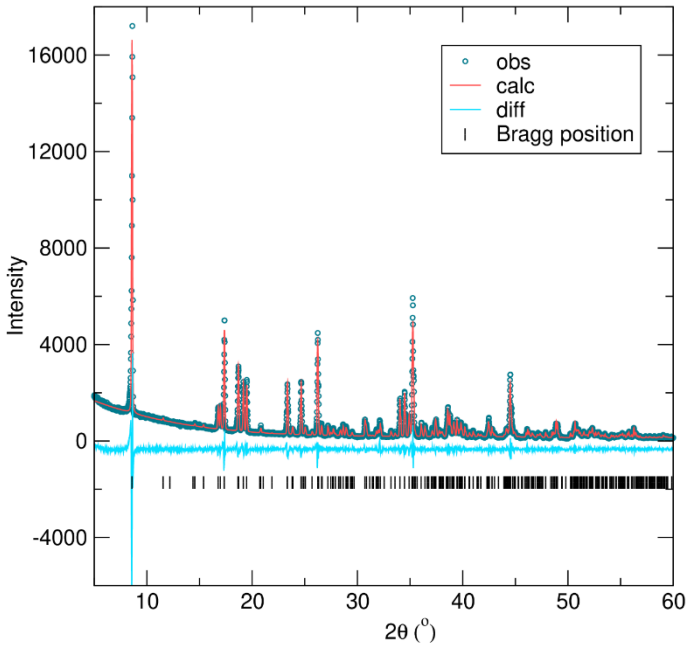

Figure S16. Simulated (form single-crystal x-ray data) and experimental PXRD patterns of $(PPDA)_2AgRuCl_8$ (**1**).

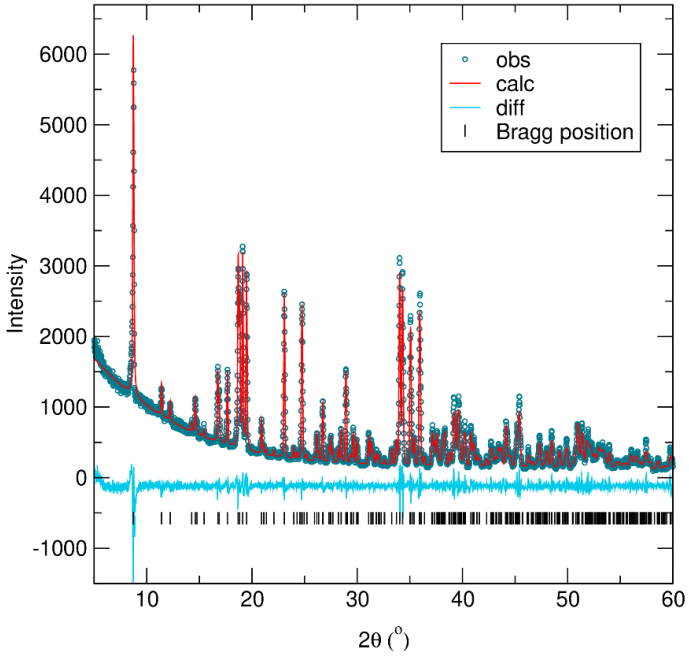

Figure S17. Simulated (form single-crystal x-ray data) and experimental PXRD patterns of $(PPDA)_2CuRuCl_8$ (**2**).

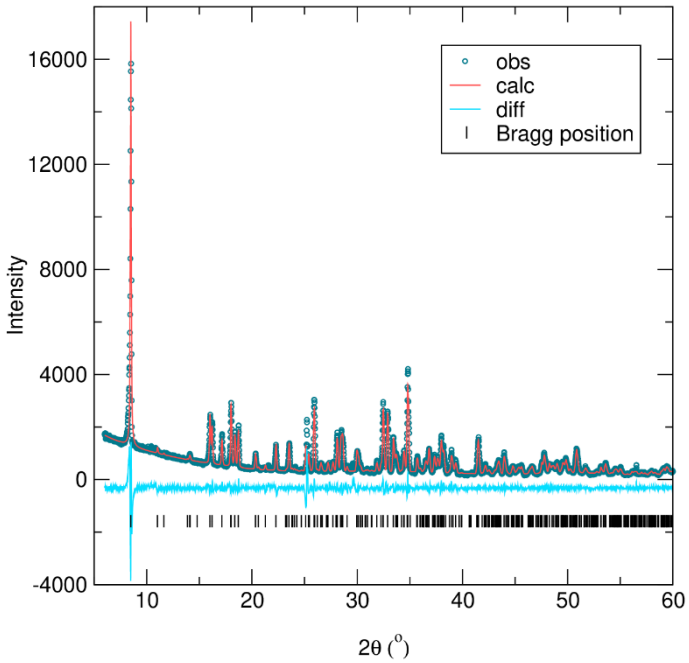

Figure S18. Simulated (form single-crystal x-ray data) and experimental PXRD patterns of $(PPDA)_2AgRuBr_8$ (**3**).

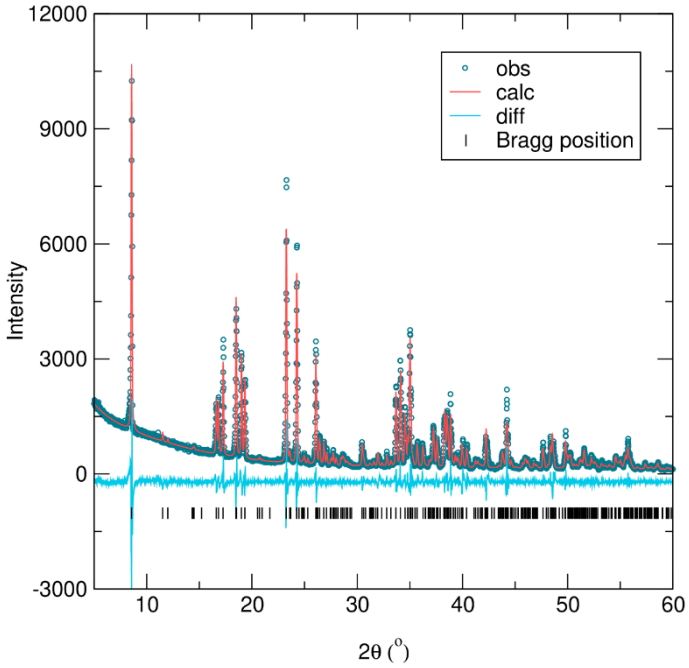

Figure S19. Simulated (form single-crystal x-ray data) and experimental PXRD patterns of $(PPDA)_2AgMoCl_8$ (**4**).

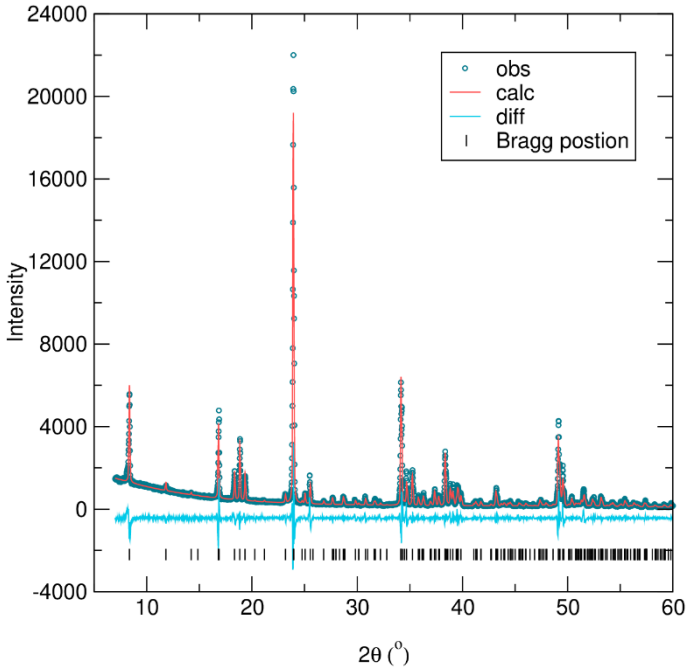

Figure S20. Simulated (form single-crystal x-ray data) and experimental PXRD patterns of (1,4-BDA)$_2$AgRuCl$_8$ (**5**).

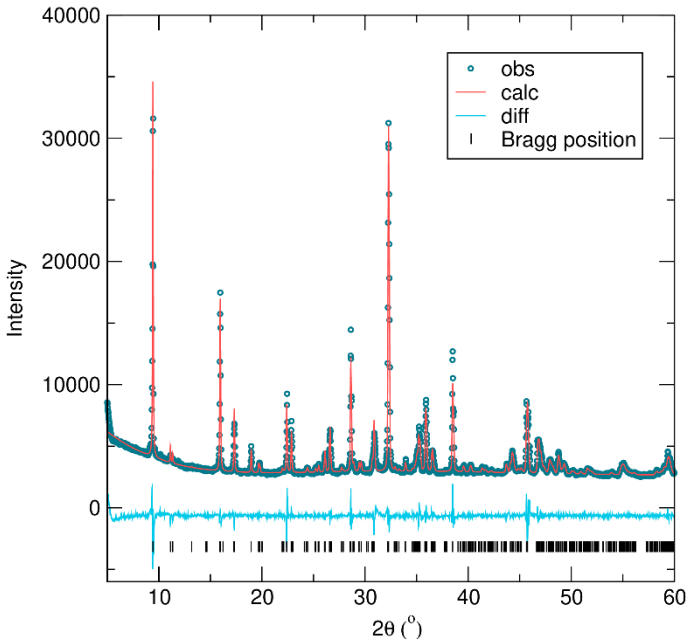

Figure S21. Simulated (form single-crystal X-ray structure) and experimental PXRD patterns of (1,4-BDA)$_2$AgRuBr$_8$ (**6**).

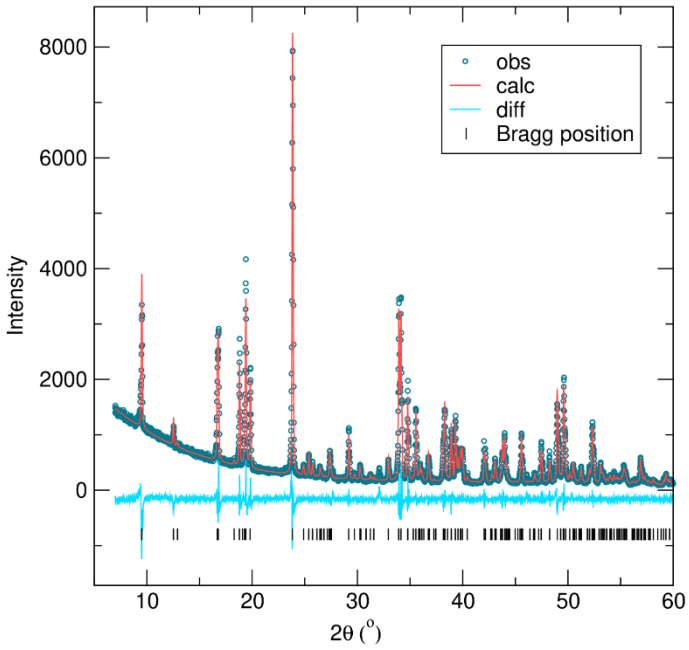

Figure S22. Simulated (form single-crystal x-ray data) and experimental PXRD patterns of (1,3-PDA)$_2$AgRuCl$_8$ (**7**).

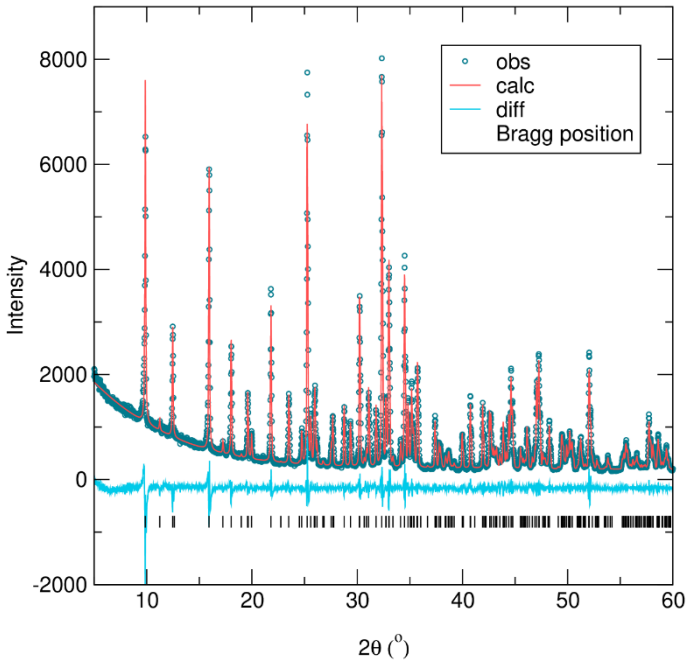

Figure S23. Simulated (form single-crystal X-ray structure) and experimental PXRD patterns of (1,3-PDA)$_2$AgRuBr$_8$ (**8**).

Table S7. Comparison of unit cell lengths (Å) angles (°) obtained from scXRD (black) and Le Bail fitting of the PXRD patterns (red).

$(PPDA)_2AgRuCl_8$ (1)		**$(1,4\text{-}BDA)_2AgRuCl_8$ (5)**	
scXRD	***PXRD***	***scXRD***	***PXRD***
a = 7.186(3)	*a* = 7.19718	*a* = 10.465(3)	*a* = 10.47136
b = 7.561(3)	*b* = 7.57783	*b* = 10.413(3)	*b* = 10.45441
c = 10.160(4)	*c* = 10.15984	*c* = 10.424(3)	*c* = 10.42083
α = 90.703(11)	α = 90.656	α = 90	α = 90
β = 93.266(11)	β = 93.221	β = 93.722(12)	β = 93.697
γ = 90.747(12)	γ = 90.677	γ = 90	γ = 90
$(PPDA)_2CuRuCl_8$ (2)		**$(1,4\text{-}BDA)_2AgRuBr_8$ (6)**	
scXRD	***PXRD***	***scXRD***	***PXRD***
a = 7.160(2)	*a* = 7.1496	*a* = 7.930(7)	*a* = 7.91782
b = 7.659(2)	*b* = 7.65713	*b* = 7.949(7)	*b* = 7.93434
c = 9.972(3)	*c* = 9.96055	*c* = 9.556(8)	*c* = 9.54187
α = 91.307(8)	α = 91.336	α = 101.870(12)	α = 101.887
β = 92.633(10)	β = 92.665	β = 90.325(13)	β = 90.369
γ = 90.482(7)	γ = 90.386	γ = 90.042(13)	γ = 90.089
$(PPDA)_2AgRuBr_8$ (3)		**$(1,3\text{-}PDA)_2AgRuCl_8$ (7)**	
scXRD	***PXRD***	***scXRD***	***PXRD***
a = 7.525(9)	*a* = 7.52937	*a* = 10.492(5)	*a* = 10.52825
b = 7.919(10)	*b* = 7.93194	*b* = 10.433(5)	*b* = 10.4535
c = 10.262(13)	*c* = 10.27719	*c* = 10.249(5)	*c* = 10.27357
α = 91.12(3)	α = 90.815	α = 90	α = 90
β = 92.55(3)	β = 92.681	β = 117.257(11)	β = 117.3237
γ = 90.71(3)	γ = 90.667	γ = 90	γ = 90
$(PPDA)_2AgMoCl_8$(4)		**$(1,3\text{-}PDA)_2AgRuBr_8$ (8)**	
scXRD	***PXRD***	***scXRD***	***PXRD***
a = 7.583(7)	*a* = 7.31974	*a* = 18.569(6)	*a* = 18.55811
b = 7.583(7)	*b* = 7.61476	*b* = 7.519(3)	*b* = 7.15565
c = 10.194(15)	*c* = 10.23009	*c* = 8.168(3)	*c* = 8.16423
α = 91.12(3)	α = 90.714	α = 90	α = 90
β = 93.66(3)	β = 93.307	β = 108.113(7)	β = 108.126
γ = 90.96(5)	γ = 90.665	γ = 90	γ = 90

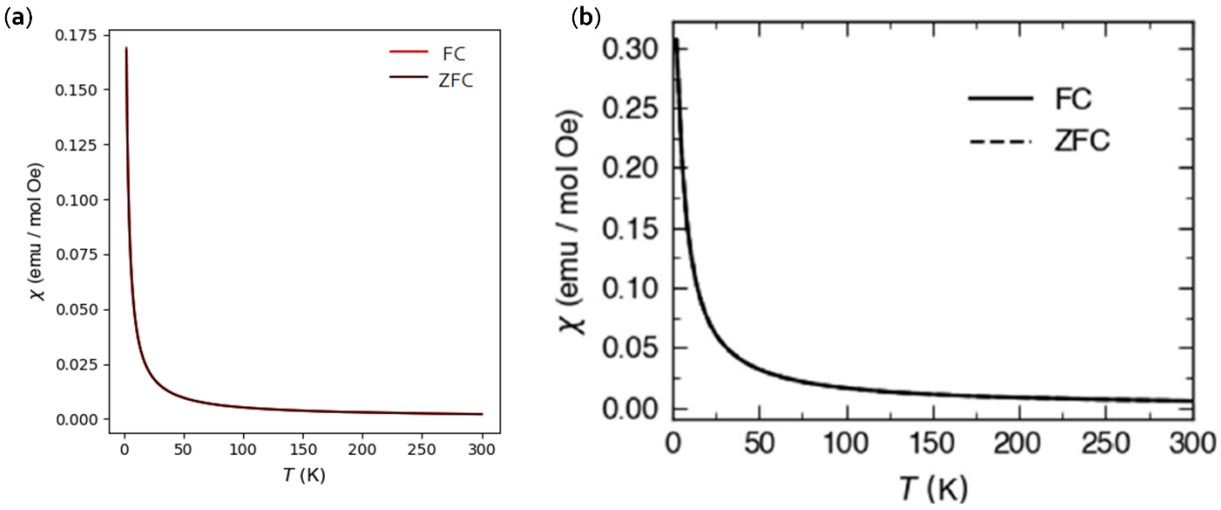

Figure S24. The magnetic susceptibilities of (a) $(PPDA)_2AgRuCl_8$ (**1**) and (b) $(PPDA)_2AgMoCl_8$ (**4**), measured between 2 K and 300 K.

References:

(S1) Sheldrick, G. M. Crystal Structure Refinement with *SHELXL*. *Acta Crystallogr. Sect. C* **2015**, *71*, 3–8.

(S2) Momma, K.; Izumi, F. *VESTA* 3 for Three-Dimensional Visualization of Crystal, Volumetric and Morphology Data. *J. Appl. Crystallogr.* **2011**, *44*, 1272–1276.

(S3) Toby, B. H.; Von Dreele, R. B. *GSAS-II*: The Genesis of a Modern Open-Source All Purpose Crystallography Software Package. *J. Appl. Crystallogr.* **2013**, *46*, 544–549.

(S4) Lassoued, M. S.; Bi, L.-Y.; Wu, Z.; Zhou, G.; Zheng, Y.-Z. Piperidine-Induced Switching of the Direct Band Gaps of Ag(I)/Bi(III) Bimetallic Iodide Double Perovskites. *J. Mater. Chem. C* **2020**, *8*, 5349–5354.

(S5) Li, X.; Traoré, B.; Kepenekian, M.; Li, L.; Stoumpos, C. C.; Guo, P.; Even, J.; Katan, C.; Kanatzidis, M. G. Bismuth/Silver-Based Two-Dimensional Iodide Double and One-Dimensional Bi Perovskites: Interplay between Structural and Electronic Dimensions. *Chem. Mater.* **2021**, *33*, 6206–6216.

(S6) Bi, L.-Y.; Hu, Y.-Q.; Li, M.-Q.; Hu, T.-L.; Zhang, H.-L.; Yin, X.-T.; Que, W.-X.; Lassoued, M. S.; Zheng, Y.-Z. Two-Dimensional Lead-Free Iodide-Based Hybrid Double Perovskites: Crystal Growth, Thin-Film Preparation and Photocurrent Responses. *J. Mater. Chem. A* **2019**, *7*, 19662–19667.

(S7) Bi, L.-Y.; Hu, T.-L.; Li, M.-Q.; Ling, B.-K.; Lassoued, M. S.; Hu, Y.-Q.; Wu, Z.; Zhou, G.; Zheng, Y.-Z. Template Effects in Cu(I)–Bi(III) Iodide Double Perovskites: A Study of Crystal Structure, Film Orientation, Band Gap and Photocurrent Response. *J. Mater. Chem. A* **2020**, *8*, 7288–7296.

(S8) Fu, D.; Wu, S.; Liu, Y.; Yao, Y.; He, Y.; Zhang, X.-M. A Lead-Free Layered Dion–Jacobson Hybrid Double Perovskite Constructed by an Aromatic Diammonium Cation. *Inorg. Chem. Front.* **2021**, *8*, 3576–3580.

(S9) Mao, L.; Teicher, S. M. L.; Stoumpos, C. C.; Kennard, R. M.; DeCrescent, R. A.; Wu, G.; Schuller, J. A.; Chabinyc, M. L.; Cheetham, A. K.; Seshadri, R. Chemical and Structural Diversity of Hybrid Layered Double Perovskite Halides. *J. Am. Chem. Soc.* **2019**, *141*, 19099–19109.

(S10) Ruan, H.; Guo, Z.; Lin, J.; Liu, K.; Guo, L.; Chen, X.; Zhao, J.; Liu, Q.; Yuan, W. Structure and Optical Properties of Hybrid-Layered-Double Perovskites $(C_8H_{20}N_2)_2AgMBr_8$ (M = In, Sb, and Bi). *Inorg. Chem.* **2021**, *19*, 14629–14635.

(S11) Jana, M. K.; Janke, S. M.; Dirkes, D. J.; Dovletgeldi, S.; Liu, C.; Qin, X.; Gundogdu, K.; You, W.; Blum, V.; Mitzi, D. B. Direct-Bandgap 2D Silver–Bismuth Iodide Double Perovskite: The Structure-Directing Influence of an Oligothiophene Spacer Cation. *J. Am. Chem. Soc.* **2019**, *141*, 7955–7964.

(S12) Castro-Castro, L. M.; Guloy, A. M. Organic-Based Layered Perovskites of Mixed-Valent Gold(I)/Gold(III) Iodides. *Angew. Chem. Int. Ed.* **2003**, *42*, 2771–2774.

(S13) Sun, B.; Liu, X.-F.; Li, X.-Y.; Zhang, Y.; Shao, X.; Yang, D.; Zhang, H.-L. Two-Dimensional Perovskite Chiral Ferromagnets. *Chem. Mater.* **2020**, *32*, 8914–8920.

(S14) Robinson, K.; Gibbs, G. V; Ribbe, P. H. Quadratic Elongation: A Quantitative Measure of Distortion in Coordination Polyhedra. *Science (80-.).* **1971**, *172*, 567–570.